

Three-phase mixed-wet capillary pressure curves from a bundle-of-triangular-tubes model

Johan O. Helland^{*}, Svein M. Skjæveland

University of Stavanger, N-4036 Stavanger, Norway

Abstract

We present a bundle-of-triangular-tubes model that simulates three-phase mixed-wet capillary pressure curves for any sequences of gas, oil, and water invasion processes. A diversity of cross-sectional fluid configurations may occur because of pore shape and different combinations of the contact angles. We use expressions for the capillary entry pressures that truly accounts for the mixed wettability condition and the possibility of simultaneous displacement of the fluids occupying the cross-sections. As a consequence, invasion does not necessarily proceed in the order of monotonic increasing or decreasing pore size. We simulate primary drainage and imbibition first. The saturation dependencies of the three-phase capillary pressures are analyzed for the subsequent gas injections and waterfloods and compared with the results from a similar bundle-of-cylindrical-tubes model. Simulations are performed for three sets of contact angles representing oil-wet conditions with variable contact angle hysteresis. It is shown that the capillary pressure at the end of primary drainage, P_{cow}^{\max} , strongly affects the saturation dependencies in the bundle of triangular tubes. For moderate values of P_{cow}^{\max} , we have identified regions in the saturation space where *two* or all *three* capillary pressures are functions of two saturations, while the corresponding results from the bundle of cylindrical tubes show that only one of the capillary pressures depends on more than one saturation, regardless of P_{cow}^{\max} . The differences are caused by the capillary entry pressures in the triangular tubes that are strongly affected by the hinging interfaces in the corners when contact angle hysteresis is assumed. This leads to different bulk pore occupancies in the two bundle models, and hence different saturation dependencies. Furthermore, the level of gas-water and oil-water capillary pressure is higher for the bundle of triangular tubes during the gas and water invasion processes. The saturation dependencies, capillary levels and pore occupancies calculated from triangular tubes approach the corresponding results calculated from cylindrical tubes when P_{cow}^{\max} is increased.

Key words: Three-phase; Mixed wettability; Triangular tubes; Capillary pressure

^{*} Corresponding author. Tel.: +47-5183-2222; fax: +47-5183-1050
Email address: johan.o.helland@uis.no (Johan O. Helland).

1 Introduction

To describe three-phase transition zones and the dynamics of water-oil and gas-oil contact movements, a three-phase capillary pressure correlation is needed for mixed-wet reservoirs. The correlation should be based on sound physical principles yet sufficiently simple to be included in a reservoir simulator. In the reservoir, situations may occur where one of the phases appears or disappears, e.g., transitions between gas and oil phase in condensate reservoirs, or when zero residual oil saturation is approached by drainage through connected layers. The correlation should be designed to account for a smooth transition between two- and three-phase flow to accommodate these situations.

Three-phase capillary pressure vs. saturation relationships have traditionally been predicted from corresponding two-phase measurements. However, both experimental and numerical work have shown that this approach is not always valid. Hence, there is a need for direct measurements of three-phase capillary pressure relationships to develop reliable correlations. There is a paucity of data reported in the literature. To our knowledge, measurements with three varying saturations have only been reported by Kalaydjian (1992). He measured three-phase drainage and imbibition capillary pressures in water-wet sandstone core samples. Bradford and Leij (1995a,b, 1996) measured three-phase capillary pressures in sandpacks for several wetting conditions achieved by mixing different fractions of water-wet and oil-wet sands. In these experiments, however, one saturation was kept fixed.

As there are few measured three-phase capillary data available, we have chosen the route of adding artificially generated data from a simple simulation model. Because of two independent saturations, there is an infinite number of possible three-phase displacement processes. The trajectory of a specific process in the saturation space is determined by the three capillary pressures. A simulation model that produces realistic capillary pressure curves may be used to predict processes not covered by time-consuming measurements. We choose to represent the pore network as a bundle of tubes, the tubes having triangular, equilateral cross-sections. The triangular pore shape allows for representation of physical processes such as the development of mixed wettability within a single pore (Kovscek et al., 1993; Hui and Blunt, 2000) and oil drainage through layers in the crevices (Hui and Blunt, 2000; Dong et al., 1995; Keller et al., 1997). The possibility of simultaneous occupancy of more than one fluid phase in the cross-sectional area of a triangular tube requires analysis of the fluid configurations and accurate calculation of the capillary entry pressures accounting for all possible displacements. Although a simple bundle-of-triangular-tubes model does not produce residual saturations caused by phase entrapment, we have found that main features of two-phase, mixed-wet, capillary pressure curves with scanning loops can be reproduced when contact angle hysteresis is assumed (Helland and Skjæveland, 2004a).

Recently, van Dijke and Sorbie (2003) derived a general formula for three-phase capillary entry pressures into tubes with angular cross-sections accounting for simultaneous displacement of all phases. However, they only considered pores of uniform wettability. We extend the method to account for mixed-wet tubes with contact angle hysteresis from the two-phase derivation given by Ma et al. (1996). Along with the derivations we propose an algorithm that determines which displacement to occur for different capillary pressures and combinations of the contact angles. The first version of the present paper was submitted April 26 and presented May 18 at the 8th International Symposium on Reservoir Wettability. Independently, similar work on three-phase entry pressure with contact angle hysteresis was carried out by Piri and Blunt (2004), and their results were submitted July 10 and published December 14. The authors derive a general expression for the entry pressures and study in detail gas invasion into bulk oil and oil invasion into bulk gas with water present in the corners. In this paper we describe the more complicated cases when gas invades configurations with oil layers bounded by bulk water and water in the corners, and when water invades configurations with oil layers surrounded by bulk gas and water in the corners. These two scenarios are important when water-alternate-gas (WAG) injections are simulated using mixed-wet triangular tubes.

The saturation dependencies of three-phase capillary pressures and relative permeabilities for mixed-wet conditions without contact angle hysteresis have been analyzed by van Dijke et al. (2001a,b) using a bundle of cylindrical tubes. They identified three regions in the saturation space where the capillary pressures have different saturation dependencies. In each region only one of the capillary pressures depends on more than one saturation. However, this may not be true if contact angle hysteresis is assumed as other pore occupancies than those analyzed by van Dijke et al. (2001a,b) can occur. Very recently, van Dijke and Sorbie (2005) compared the displacement paths and saturation dependencies from the bundle of cylindrical tubes with the corresponding results from a bundle of triangular tubes without contact angle hysteresis. The results were in good agreement.

In the present paper, we describe the three-phase bundle-of-triangular-tubes model. Three-phase capillary pressure vs. saturation relationships are calculated for gas injection followed by waterflooding when contact angle hysteresis is assumed. The gas phase is introduced after the first imbibition. For this sequence of processes we investigate if the three-phase entry pressures are sensitive to the capillary pressures at the end of the preceding invasion process and to the capillary pressure where primary drainage was terminated, P_{cow}^{\max} . The saturation dependencies of the capillary pressures during the gas and water injections are analyzed and compared with the results from a similar model of cylindrical tubes. The effect of P_{cow}^{\max} on the saturation dependencies is also explored.

2 Preliminaries

The wetting preference of a solid surface in contact with two fluids is typically characterized by the contact angle. Assuming that the denser phase j is wetting relative to phase i , then $\cos \theta_{ij} \geq 0$, where the contact angle θ_{ij} is measured through phase j . The wetting order in a three-phase fluid system of oil, water and gas may be divided into three categories (Hui and Blunt, 2000; Zhou and Blunt, 1998):

- In water-wet media, water is wetting, oil intermediate-wetting, and gas non-wetting. The contact angles satisfy $\theta_{ow} \leq \frac{\pi}{2}$, $\theta_{go} \leq \frac{\pi}{2}$, and $\theta_{gw} \leq \frac{\pi}{2}$.
- In weakly oil-wet media, oil is wetting, water intermediate-wetting, and gas non-wetting ($\theta_{ow} > \frac{\pi}{2}$, $\theta_{go} \leq \frac{\pi}{2}$, and $\theta_{gw} \leq \frac{\pi}{2}$).
- In strongly oil-wet media, oil is wetting, gas intermediate-wetting, and water non-wetting ($\theta_{ow} > \frac{\pi}{2}$, $\theta_{go} \leq \frac{\pi}{2}$, and $\theta_{gw} > \frac{\pi}{2}$).

Recently, van Dijke and Sorbie (2002b) proposed linear relationships of $\cos \theta_{go}$ and $\cos \theta_{gw}$ as functions of $\cos \theta_{ow}$ accounting for the above wetting orders:

$$\cos \theta_{go} = \frac{1}{2\sigma_{go}}(C_{so} \cos \theta_{ow} + C_{so} + 2\sigma_{go}), \quad (1)$$

and

$$\cos \theta_{gw} = \frac{1}{2\sigma_{gw}}((C_{so} + 2\sigma_{ow}) \cos \theta_{ow} + C_{so} + 2\sigma_{go}), \quad (2)$$

where the oil spreading coefficient $C_{so} = \sigma_{gw} - \sigma_{go} - \sigma_{ow}$ is nonpositive and reflects the interfacial tensions measured at thermodynamic equilibrium. Thus assuming that the underlying wettability is known in terms of the oil-water contact angles, calculations of θ_{go} and θ_{gw} are possible by Eqs. (1), (2).

An important feature of the capillary behavior in an angular tube is the possibility of simultaneous occupancy of more than one fluid in the cross-section. The prevailing cross-sectional fluid configuration depends on the pore shape, the contact angles, and the capillary pressures. Expressions for the two-phase capillary entry pressures are derived by the MS-P method, named after the contributions from Mayer and Stowe (1965) and Princen (1969a,b, 1970). This method is founded on an energy balance equation which equates the virtual work with the associated change of surface free energy for a small displacement of the interface in the direction along the tube. The energy balance equation then relates the entry radius of curvature to the cross-sectional area exposed to change of fluid occupancy, the bounding cross-sectional fluid-solid and fluid-fluid lengths, and the contact angle.

Following this approach, Ma et al. (1996) derived the capillary entry pressures for primary drainage and imbibition for mixed-wet, regular, n -sided tubes. The analysis for this geometry is largely simplified as all corners have the same half-angle α and hence the same fluid configuration. There are two scenarios that need to be

considered separately depending on the contact angle. As an example, consider invasion of phase i into a uniformly wetted tube initially filled with the denser phase j . If

$$\theta_{ij} < \frac{\pi}{2} - \alpha, \quad (3)$$

phase i occupies the bulk area while phase j is still residing in the corners. If the contact angle does not satisfy Eq. (3), phase i occupies the entire cross-section during invasion. The invading interface separating the bulk fluids is referred to as the main terminal meniscus (MTM), and the interface separating bulk fluid from corner fluid, if present, is referred to as the arc meniscus (AM). The curvature of an AM is represented by a cross-sectional circular arc of radius r_{ij} . Thus, by Laplace's equation, the capillary pressure may be expressed as

$$P_{cij} = \frac{\sigma_{ij}}{r_{ij}}. \quad (4)$$

In a three-phase system the capillary pressures are, by definition, related to each other by

$$P_{cgw} = P_{cgo} + P_{cow}. \quad (5)$$

The application of Eq. (4) on all capillary pressures then yields the useful relation

$$\frac{\sigma_{gw}}{r_{gw}} = \frac{\sigma_{go}}{r_{go}} + \frac{\sigma_{ow}}{r_{ow}}. \quad (6)$$

Hence, if two of the radii of curvature are known, we may calculate the third from Eq. (6).

3 Model description

The pore network is represented as a bundle of parallel tubes, the tubes having equilateral, triangular cross-sections. The geometry of an equilateral triangle is readily described by the half-angle of the corner, $\alpha = \frac{\pi}{6}$, and the radius of the inscribed circle R . We assume that the pore-size frequency is described by a truncated two-parameter Weibull distribution. This is a flexible distribution that has been employed frequently for this purpose (Diaz et al., 1987; Fenwick and Blunt, 1998; Hui and Blunt, 2000). The pore sizes R are selected from the cumulative distribution function in the following manner: Pick random numbers $x \in [0, 1]$ and calculate the inscribed radius from

$$R = R_{\text{ch}} \left(-\ln[(1-x) \exp(-\left[\frac{R_{\text{max}} - R_{\text{min}}}{R_{\text{ch}}}\right]^\eta) + x] \right)^{\frac{1}{\eta}} + R_{\text{min}}, \quad (7)$$

where R_{max} , R_{min} and R_{ch} are the inscribed radii of the largest, smallest and characteristic pore sizes, respectively, and η is a dimensionless parameter.

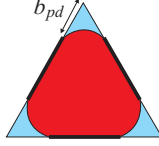


Figure 1. Final configuration of a tube after primary drainage. The bold lines along the sides represent the lengths of the pore wall where the wettability may have changed. The distances b_{pd} in the corners remain water-wet.

The model is programmed to simulate gas, oil and water invasion processes in any sequence starting with primary drainage of a waterfilled and water-wet medium. An invasion process is simulated by increasing or decreasing a capillary pressure stepwise until some maximum or minimum value is reached. At each step the fluid occupancies in the tubes are updated and the saturation is calculated. The saturations are calculated based on the fraction of the cross-sectional area that each phase occupies. Invasion of the oil phase is simulated by increasing P_{cow} at a constant P_{cgo} . At each pressure step P_{cgo} is calculated from Eq. (5). During water invasion P_{cow} is decreased at a constant P_{cgo} , and P_{cgo} is calculated by Eq. (5). During gas invasion P_{cgo} is increased, and P_{cgo} is calculated from Eq. (5) assuming a constant P_{cow} . To simulate a predetermined sequence of several gas, oil and water invasion processes, a list of capillary pressures is specified where each value corresponds to the capillary pressure at which the specific process is terminated.

Initially all tubes are waterfilled and strongly water-wet, and hence the contact angle during primary drainage, θ_{pd} , is always small and satisfies Eq. (3). It is assumed that oil always contacts the pore walls of the invaded tubes, and hence the sides may experience a wettability alteration while the corners remain water-wet. The final configuration of a tube after primary drainage is shown in Fig. 1. The distance b_{pd} of the solid surface that remains water-wet is given by

$$b_{pd} = \frac{\sigma_{ow} \cos(\theta_{pd} + \alpha)}{P_{cow}^{\max} \sin \alpha}, \quad (8)$$

where P_{cow}^{\max} is the capillary pressure at the end of primary drainage. Irreducible water saturations caused by phase entrapment do not occur in the model as we only consider a bundle of tubes. However, we may argue that a legitimate value of P_{cow}^{\max} is reached if the next pressure increase results in a saturation change smaller than some tolerance value.

The amount of contact angle hysteresis between primary drainage, imbibition and secondary drainage is affected by the degree of wettability alteration and the surface roughness (Morrow, 1975; Yang et al., 1999). To accommodate this we allow all receding and advancing oil-water contact angles, θ_{owr} and θ_{owa} respectively, that satisfy $\theta_{pd} \leq \theta_{owr} \leq \theta_{owa}$. If gas displaces oil and water, the gas-oil and gas-water interfaces are receding with contact angles θ_{gor} and θ_{gwr} calculated from Eqs. (1), (2) with $\theta_{ow} = \theta_{owr}$. Similarly, oil and water displaces gas with advancing contact angles θ_{goa} and θ_{gwa} calculated from Eqs. (1), (2) assuming $\theta_{ow} = \theta_{owa}$.

4 Fluid configurations

The model allows for simulations of any sequence of the invasion processes starting with primary drainage. Contact angle hysteresis then leads to a diversity of possible fluid configurations that have to be analyzed individually. The number of configurations are restricted by the following assumptions:

- (i) We only consider the three aforementioned wetting orders.
- (ii) We allow maximum two AMs to be present on the surface exposed to a potential wettability change. An additional AM may be located at position b_{pd} .
- (iii) We do not study situations where the gas pressure is large enough for gas invasion into tubes, and corners of tubes, where oil has never been.

With these constraints we find that the 17 configurations presented in Fig. 2 may occur during the simulations. Configuration A shows a tube that has always been waterfilled and water-wet. The configurations B–Q represent tubes that at some point have been invaded by oil and thus may have altered wettability. The curvatures of the gas-oil interfaces present in the configurations are always positive, whereas the gas-water and oil-water interfaces may have positive or negative curvatures to satisfy Eq. (5). In Table 1 we have specified the combinations of receding and advancing contact angles for which the different fluid configurations may occur. Contact angles are also specified to discriminate between the three wetting sequences whenever it is possible. Three-phase fluid configurations in mixed-wet angular tubes have previously been analyzed by Piri and Blunt (2002, 2004, 2005). As opposed to us, they also consider cases where gas is wetting relative to oil. However, they have not accounted for our configurations F and K, which may occur when contact angle hysteresis is large. To our knowledge, only the configurations A–D, H, I, M and N have been observed by experiments in triangular tubes or in micromodels (e.g., Dong et al., 1995; Dong and Chatzis, 1995; Zhou et al., 1997; Keller et al., 1997; Spildo and Buckley, 1999).

Assumption (i) implies that oil is always wetting relative to gas, i.e., $\theta_{go} < \frac{\pi}{2}$. Hence, bulk oil can not be bounded by gas layers in the cross-sections. Assumption (ii) is introduced to restrict the number of AMs in cases where contact angle hysteresis is large. If

$$\theta_{ija} > \frac{\pi}{2} + \alpha \quad \text{and} \quad \theta_{ijr} < \frac{\pi}{2} - \alpha, \quad ij = ow, gw, \quad (9)$$

it is possible, in theory, that the number of AMs present in a cross-section could increase constantly as the number of saturation change reversals increases. For example, if Eq. (9) is satisfied for the oil-water contact angles, water invasion into configuration C may be a displacement to configuration E, while oil invasion into configuration E may be a displacement to configuration F. A subsequent water invasion into configuration F could then result in formation of a fourth AM in the

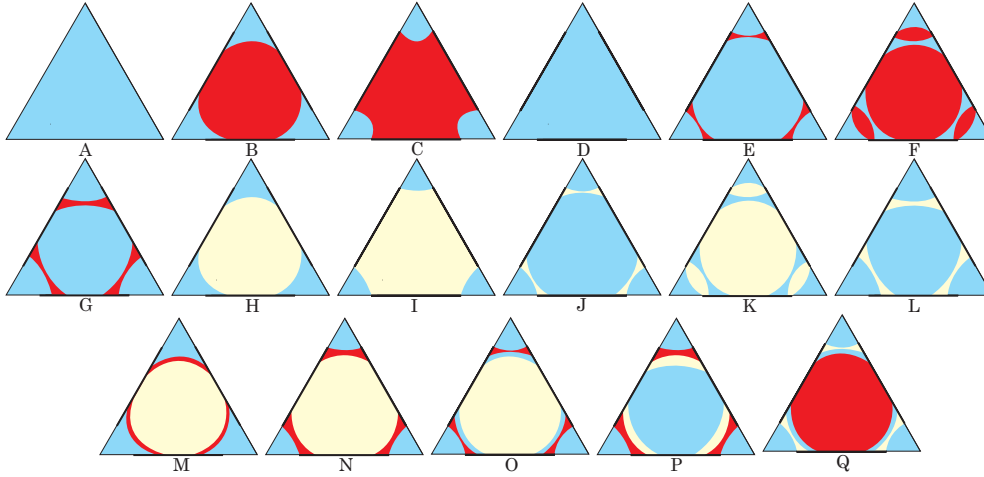


Figure 2. Fluid configurations for any sequences of the invasion processes, with water in blue, oil in red, and gas in yellow. The bold lines along the sides represent the lengths with potentially altered wettability. Oil is always assumed to be wetting relative to gas.

corner, separating bulk water from a second oil layer. Even though Eq. (9) is satisfied, we do not allow formation of a new AM in the corner when two AMs are already present on the surface of altered wettability, by assumption (ii). We believe that this simplification is reasonable, since new AMs are likely to interfere with the AMs already present in most of these cases. Hence, water invasion into the bulk of configuration F is always assumed to be a displacement from configuration F to E.

This sequence of oil-water displacements can only occur if the tube behaves as oil-wet during waterflooding and as water-wet during oil invasion. Similar configuration changes may occur during the gas-water displacements if Eq. (9) is satisfied for both the gas-water and the oil-water contact angles, i.e., when the tube behaves as *strongly oil-wet* during waterflooding and as water-wet during gas invasion. Notice from Table 1 that the configurations F, G, K, L and Q can only occur if the wetting sequence of the three phases changes with the direction of the displacement. We allow for such capillary behavior since measurements indicate that contact angle hysteresis may be large if wettability alteration has occurred (Yang et al., 1999). Furthermore, this effect may be more common when irregular geometries with different corner half angles α are assumed, since the contact angle hysteresis required to satisfy Eq. (9) are smaller in narrow corners.

By assumption (iii), we do not allow for invasion of gas-water interfaces onto the water-wet surface where oil has never been, since we believe that the most realistic cases of three-phase flow in reservoirs can be studied without including this feature in the model. Nevertheless, such displacements could be accounted for by specifying gas-water and gas-oil contact angles on the water-wet surface as well, although this would increase the number of configurations. Assumption (iii) implies that any gas-water AMs located at position b_{pd} are hinging with contact angles varying with P_{cgw} . Oil-water AMs located at this position are allowed to move on to the water-wet surface when the hinging contact angle has reached θ_{pd} . This happens when

Configuration	θ_{owa}	θ_{owr}	θ_{gwa}	θ_{gwr}	θ_{goa}	θ_{gor}
A	n/a	n/a	n/a	n/a	n/a	n/a
B	–	$< \frac{\pi}{2} - \alpha$	–	$\leq \frac{\pi}{2}$	$\leq \frac{\pi}{2}$	$\leq \frac{\pi}{2}$
C	–	–	–	–	$\leq \frac{\pi}{2}$	$\leq \frac{\pi}{2}$
D	–	–	–	–	$\leq \frac{\pi}{2}$	$\leq \frac{\pi}{2}$
E	$> \frac{\pi}{2} + \alpha$	–	–	–	$\leq \frac{\pi}{2}$	$\leq \frac{\pi}{2}$
F	$> \frac{\pi}{2} + \alpha$	$< \frac{\pi}{2} - \alpha$	–	$\leq \frac{\pi}{2}$	$\leq \frac{\pi}{2}$	$\leq \frac{\pi}{2}$
G	$> \frac{\pi}{2} + \alpha$	$< \frac{\pi}{2} - \alpha$	–	$\leq \frac{\pi}{2}$	$\leq \frac{\pi}{2}$	$\leq \frac{\pi}{2}$
H	–	–	–	$< \frac{\pi}{2} - \alpha$	$\leq \frac{\pi}{2}$	$\leq \frac{\pi}{2}$
I	–	–	–	–	$\leq \frac{\pi}{2}$	$\leq \frac{\pi}{2}$
J	$> \frac{\pi}{2}$	–	$> \frac{\pi}{2} + \alpha$	–	$\leq \frac{\pi}{2}$	$\leq \frac{\pi}{2}$
K	$> \frac{\pi}{2}$	–	$> \frac{\pi}{2} + \alpha$	$< \frac{\pi}{2} - \alpha$	$\leq \frac{\pi}{2}$	$\leq \frac{\pi}{2}$
L	$> \frac{\pi}{2}$	–	$> \frac{\pi}{2} + \alpha$	$< \frac{\pi}{2} - \alpha$	$\leq \frac{\pi}{2}$	$\leq \frac{\pi}{2}$
M	–	$< \frac{\pi}{2} - \alpha$	–	$\leq \frac{\pi}{2}$	$\leq \frac{\pi}{2}$	$< \frac{\pi}{2} - \alpha$
N	–	–	–	–	$\leq \frac{\pi}{2}$	$< \frac{\pi}{2} - \alpha$
O	$> \frac{\pi}{2} + \alpha$	–	–	$< \frac{\pi}{2} - \alpha$	$\leq \frac{\pi}{2}$	$\leq \frac{\pi}{2}$
P	$> \frac{\pi}{2}$	–	$> \frac{\pi}{2} + \alpha$	–	$\leq \frac{\pi}{2}$	$< \frac{\pi}{2} - \alpha$
Q	$> \frac{\pi}{2}$	$< \frac{\pi}{2} - \alpha$	$> \frac{\pi}{2} + \alpha$	$\leq \frac{\pi}{2}$	$\leq \frac{\pi}{2}$	$\leq \frac{\pi}{2}$

Table 1

Advancing and receding contact angles for which the cross-sectional fluid configurations are possible. It is always assumed that $\theta_{pd} < \frac{\pi}{2} - \alpha$. Contact angles are also specified to associate the configurations to the three wettability orderings, if possible. Empty spaces indicate that all values satisfying $\theta_{ja} \geq \theta_{ij}$, $ij = go, ow, gw$ are allowed.

$P_{cow} = P_{cow}^{\max}$, and a further increase of P_{cow} causes the length of the water-wet surface, b_{pd} , to decrease additionally.

The AMs located on the surface of altered wettability may also hinge at fixed positions while the contact angles change with capillary pressure. The contact angles hinge according to

$$\theta_{ijh} = \begin{cases} \arccos\left(\frac{P_{cij}b_{ij} \sin \alpha}{\sigma_{ij}}\right) - \alpha & \text{if bulk phase } i \text{ is bounded} \\ & \text{by corner phase } j, \\ \arccos\left(\frac{P_{cij}b_{ij} \sin \alpha}{\sigma_{ij}}\right) + \alpha & \text{if bulk phase } j \text{ is bounded} \\ & \text{by corner phase } i, \end{cases} \quad (10)$$

Initial configuration	Final configuration		
	Oil invasion	Water invasion	Gas invasion
A	C	–	–
B	C	D or G	H, I or M
C	–	D or E	I or N
D	B or C	–	H or I
E	C or F	D	I, N or O
F	C	E	I, N or O
G	B	D	H, I or M
H	B or C	D or L	I
I	C	D or J	–
J	C or Q	D	I or K
K	C or Q	J	I
L	B or C	D	H
M	B or N	D, G or H	H
N	C	D, E, I, M or P	I
O	C, F or N	E or H	N
P	C or E	E or J	J or N
Q	C	B or J	I or K

Table 2

The programmed direct displacements during the oil, water and gas invasion processes.

where $ij = go, ow, gw$, and b_{ij} is the distance from the apex of the corner to the three-phase contact line. If the advancing or receding contact angle is reached, the AMs begin to move at constant contact angles during a further change of capillary pressure. The position b_{ij} is then changing according to

$$b_{ij} = \begin{cases} \frac{\sigma_{ij} \cos(\theta_{ij} + \alpha)}{P_{cij} \sin \alpha} & \text{if bulk phase } i \text{ is bounded by corner phase } j, \\ \frac{\sigma_{ij} \cos(\theta_{ij} - \alpha)}{P_{cij} \sin \alpha} & \text{if bulk phase } j \text{ is bounded by corner phase } i, \end{cases} \quad (11)$$

where θ_{ij} is equal to θ_{ijr} or θ_{ija} depending on the direction of the displacement.

All the direct displacements implemented in the model are presented in Table 2, including piston-like invasion, collapse of fluid layers and change of the fluid areas in the corners. The configurations A–G may appear during the two-phase oil-water displacements. Helland and Skjæveland (2004a) provided a detailed description of

the two-phase oil-water invasion processes, including expressions for the capillary entry pressures and the layer collapse capillary pressures. If the oil saturation has become zero, and only gas and water invasion processes are considered, the treatment of configuration H–L is analogous to the corresponding two-phase oil-water situation.

If piston-like invasion occur into a configuration containing multiple fluid layers in the corners, several displacements are possible, as shown in Table 2 for gas invasion into configuration F, and water invasion into configuration N for instance. Which particular displacement occurs is determined by the selected combination of contact angles and the capillary pressures. However, the number of possible displacements is reduced if the invading fluid is already present as layers. As an example, water invasion into configuration O is always a displacement to configuration E. Obviously, a direct displacement from configuration O to D is not possible since then the oil layers would have collapsed prior to MTM invasion. In that case the displacement O to H has occurred and MTM invasion must instead be considered for configuration H. The algorithm used to determine the displacements and the associated expressions for the capillary entry pressures are described in the next section for cases of gas and water invasion.

A fluid layer is assumed to collapse when the bounding AMs meet at the contact lines or the midpoints. We employ the expressions derived by Hui and Blunt (2000) for the collapse of fluid layers in a three-phase configuration. For a complete list of collapse capillary pressures we refer to Piri and Blunt (2005). The displacement resulting from water layer collapse in configuration Q is somewhat different from similar events in the other configurations since oil occupied in the bulk then becomes surrounded by gas, which is not allowed by assumption (i). However, oil is still wetting relative to gas, and thus a decreased P_{cgo} would cause spontaneous imbibition of oil into the corner and displace all of the gas phase immediately, resulting in a direct displacement from configuration Q to C. This displacement has been identified in simulations using very large contact angle hysteresis satisfying the constraints for configuration Q in Table 1.

5 Three-phase capillary entry pressures

An algorithm is formulated to determine the actual displacements occurring during piston-like invasion for all combinations of the contact angles and the capillary pressures. For each type of displacement the corresponding capillary entry pressures are calculated using the method proposed by van Dijke and Sorbie (2003). They derive three-phase capillary entry pressures from an energy balance equation which equates the virtual work W with the corresponding change in surface free energy ΔF for a small displacement δx of the MTM in the direction along the tube. The energy balance then relates the entry radius of curvature to the cross-

sectional fluid occupancy, accounting for the possibility of simultaneous displacement of the fluids occupying the cross-section. We extend their method to account for mixed wettability and contact angle hysteresis following the approach by Ma et al. (1996). Thus we incorporate the effect of hinging AMs stuck at fixed positions along the pore walls in the calculations. For two-phase flow, Helland and Skjæveland (2004a) showed that invasion does not necessarily proceed in the order of monotonic increasing or decreasing pore size when the AMs are hinging. Recently, Piri and Blunt (2004) have used the same approach to study three-phase capillary entry pressure for mixed-wet conditions and contact angle hysteresis. They consider bulk gas-oil displacements that are affected by water present in the corners, e.g., displacements between the configurations C and I. We explain how to treat the more complicated case occurring when a third phase invades a cross-section occupied by the two other phases distributed into an arbitrary number of fluid layers with one of the phases occupied in the bulk. Such displacements include gas invasion into the configurations B–G, and oil invasion into the configurations A, D and H–L. We also consider water invasion into configurations occupied by all three phases.

The conditions for layer formation is required to determine the correct displacement in each case. Formation of a new AM separating phase i from phase j at a position $b_{ij} > b_{pd}$ can only occur if the contact angles satisfy the following condition:

$$\theta_{ij} < \frac{\pi}{2} - \alpha \quad \text{if invading phase } i \text{ is bounded by corner phase } j, \quad (12a)$$

$$\theta_{ij} > \frac{\pi}{2} + \alpha \quad \text{if invading phase } j \text{ is bounded by corner phase } i, \quad (12b)$$

where $ij = go, ow, gw$, and θ_{ij} is equal to θ_{ijr} or θ_{ija} depending on the direction of the displacement. However, if Eq. (12) is not satisfied, a new AM still forms at position $b_{ij} = b_{pd}$ since then the AM is assumed to hinge with contact angle θ_{ijh} . If an AM is already present in the corner before invasion, a second condition required for layer formation is that the capillary pressure associated with the displacement must be favorable compared to the collapse capillary pressure calculated when the AMs surrounding the layer meet (van Dijke and Sorbie, 2003). According to van Dijke et al. (2004) and Piri and Blunt (2004) these two geometric conditions are necessary but not sufficient for layer formation. Using free energy principles they argue that even if the above conditions are satisfied, one should also calculate the entry pressure for the displacement without layer formation and compare it with the entry pressure for the displacement with layer formation. The actual displacement occurring is the one associated with the most favorable capillary pressure. Thus, layers form if and only if the two geometric conditions are satisfied and the displacement is the most favorable. In this work we follow van Dijke et al. (2004) and Piri and Blunt (2004) and employ all the three conditions to determine if layers form, as opposed to Helland and Skjæveland (2004a) who only used the necessary geometric conditions.

5.1 Gas into oil and water

For gas invasion into the configurations B–G, the expression for the virtual work may be written in generalized form as

$$W = \{P_{cgw}A_{gw}I_{gw} + P_{cgo}A_{go}I_{go} + (P_{cgw} - P_{cgo}) \sum_{k=N_{ow}^{fin}+1}^{N_{ow}^{init}} A_{ow}^{(k)}(-1)^k\} \delta x, \quad (13)$$

where we have applied the indicator notation of van Dijke et al. (2004),

$$I_{ij} = \begin{cases} 1 & \text{if AMs between phases } i \text{ and } j \text{ form,} \\ 0 & \text{otherwise.} \end{cases} \quad (14)$$

The cross-sectional area exposed to gas invasion is denoted A_{gw} or A_{go} if gas-water or gas-oil AMs form during the displacement, respectively. The oil-water AMs are numbered in order from the corner towards the center of the cross-section. The cross-sectional bulk area bounded by oil-water AM k is denoted $A_{ow}^{(k)}$. The total number of oil-water AMs is N_{ow}^{init} before gas invasion and N_{ow}^{fin} afterwards. Thus we always have $N_{ow}^{init} \geq N_{ow}^{fin}$.

The corresponding generalized form of the surface free energy is given by

$$\Delta F = \{(L_{fgw} + L_{sgw} \cos \theta_{gwr})\sigma_{gw}I_{gw} + (L_{fgo} + L_{sgo} \cos \theta_{gor})\sigma_{go}I_{go} + (\sigma_{gw} \cos \theta_{gwr} - \sigma_{go} \cos \theta_{gor}) \sum_{k=N_{ow}^{fin}+1}^{N_{ow}^{init}} L_{sow}^{(k)}(-1)^k - \sigma_{ow} \sum_{k=N_{ow}^{fin}+1}^{N_{ow}^{init}} L_{fow}^{(k)}\} \delta x, \quad (15)$$

where L_{fgw} and L_{sgw} are the gas-water and gas-solid lengths, respectively, that bound area A_{gw} if gas-water AMs forms. Similarly, the lengths L_{fgo} and L_{sgo} bound area A_{go} if gas-oil AMs form instead. The lengths $L_{fow}^{(k)}$ and $L_{sow}^{(k)}$ bound the oil-water area $A_{ow}^{(k)}$.

In the following we consider gas invasion into configuration E in detail. However, Eqs. (13), (15) could easily be applied to the other oil-water configurations with appropriate values of N_{ow}^{init} and N_{ow}^{fin} . Configuration E contains two oil-water AMs, and thus $N_{ow}^{init} = 2$. The parameters of configuration E required for the derivation of the capillary entry pressures are as follows, see Fig. 3(a):

$$\beta_{ow}^{(1)} = \frac{\pi}{2} - \alpha - \theta_{owh}^{(1)}, \quad (16)$$

$$A_{ow}^{(1)} = \frac{R^2}{2 \tan \alpha} - \frac{r_{ow} b_{ow}^{(1)} \sin(\alpha + \beta_{ow}^{(1)})}{2} + \frac{r_{ow}^2 \beta_{ow}^{(1)}}{2}, \quad (17)$$

$$L_{fow}^{(1)} = r_{ow} \beta_{ow}^{(1)}, \quad (18)$$

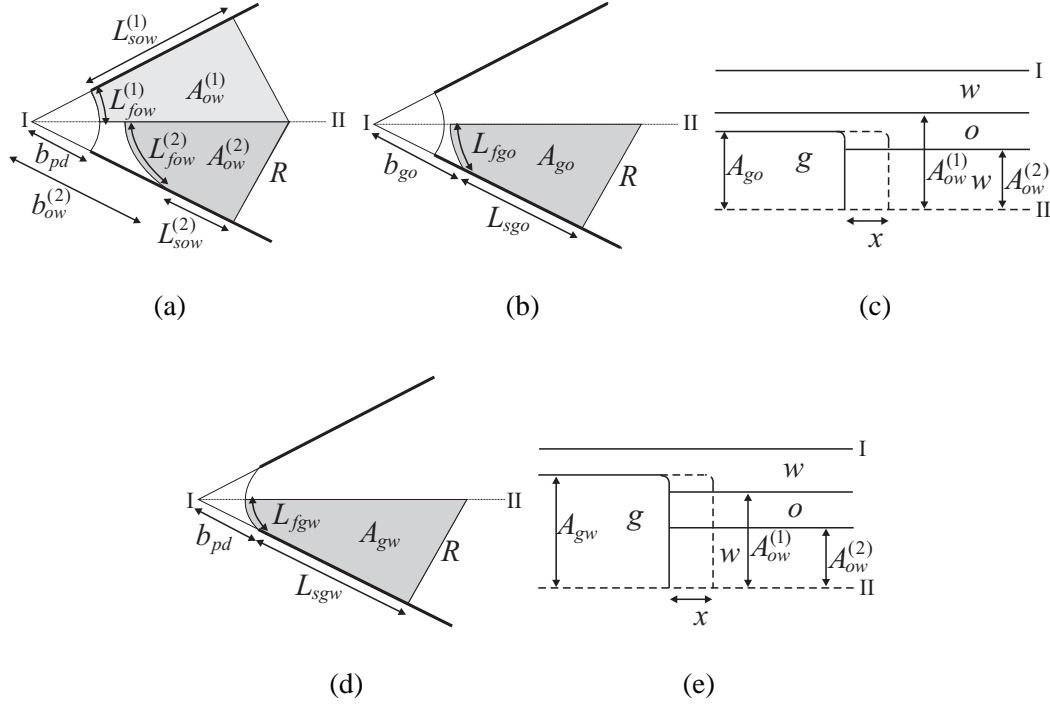


Figure 3. Representation of the cross-sectional parameters of the fluid-fluid and fluid-solid interfaces. (a) Configuration E. (b) Configuration N. (c) Displacement from configuration E to N. (d) Configuration I. (e) Displacement from configuration E to I.

$$L_{sow}^{(1)} = \frac{R}{\tan \alpha} - b_{ow}^{(1)}, \quad (19)$$

$$b_{ow}^{(1)} = \frac{r_{ow} \cos(\theta_{owh}^{(1)} + \alpha)}{\sin \alpha}, \quad (20)$$

$$\beta_{ow}^{(2)} = \frac{\pi}{2} + \alpha - \theta_{owh}^{(2)}, \quad (21)$$

$$A_{ow}^{(2)} = \frac{R^2}{2 \tan \alpha} - \frac{r_{ow} b_{ow}^{(2)} \sin(\beta_{ow}^{(2)} - \alpha)}{2} - \frac{r_{ow}^2 \beta_{ow}^{(2)}}{2}, \quad (22)$$

$$L_{fow}^{(2)} = r_{ow} \beta_{ow}^{(2)}, \quad (23)$$

$$L_{sow}^{(2)} = \frac{R}{\tan \alpha} - b_{ow}^{(2)}, \quad (24)$$

and

$$b_{ow}^{(2)} = \frac{r_{ow} \cos(\theta_{owh}^{(2)} - \alpha)}{\sin \alpha}, \quad (25)$$

where the contact angle of the innermost AM is denoted $\theta_{owh}^{(2)}$ to account for the possibility of a hinging AM before gas invasion. Moreover, $b_{ow}^{(1)} = b_{pd}$ for configuration E.

Gas invasion into configuration E is a displacement to configuration I, N or O. In configuration N and O fluid layers form during invasion. The gas-water capillary

pressure at which the water layer in configuration O collapses is given by (e.g., Piri and Blunt, 2005)

$$P_{cgw}^{col} = \begin{cases} P_{cow} \frac{\sigma_{gw} \cos \theta_{gwr} - \sin \alpha}{\sigma_{ow} \cos \theta_{owh}^{(2)} + \sin \alpha} & \text{if } \theta_{gwr} < \pi - \theta_{owh}^{(2)}, \\ P_{cow} \frac{\sigma_{gw} \cos(\theta_{gwr} + \alpha)}{\sigma_{ow} \cos(\theta_{owh}^{(2)} - \alpha)} & \text{if } \theta_{gwr} \geq \pi - \theta_{owh}^{(2)}. \end{cases} \quad (26)$$

The gas-oil capillary pressure at which the oil layer in configuration N collapses is (Piri and Blunt, 2005)

$$P_{cgo}^{col} = \begin{cases} P_{cow} \frac{\sigma_{go} \cos \theta_{gor} - \sin \alpha}{\sigma_{ow} \cos \theta_{owh}^{(1)} - \sin \alpha} & \text{if } \theta_{gor} < \theta_{owh}^{(1)}, \\ P_{cow} \frac{\sigma_{go} \cos(\theta_{gor} + \alpha)}{\sigma_{ow} \cos(\theta_{owh}^{(1)} + \alpha)} & \text{if } \theta_{gor} \geq \theta_{owh}^{(1)}. \end{cases} \quad (27)$$

We first consider the displacements and the associated capillary entry pressures when θ_{gwr} and θ_{gor} satisfy Eq. (12a). In this case the displacements to configurations I, N and O are all possible. The capillary pressures associated with these displacements are calculated first and then the actual displacement occurring is determined using the three conditions for layer formation.

For the displacement from configuration E to O Eqs. (13), (15) are applied with $N_{ow}^{fin} = 2$, $I_{go} = 0$ and $I_{gw} = 1$. By solving $W = \Delta F$, a simple two-phase expression for the gas-water capillary entry pressure is derived (e.g., Ma et al., 1996):

$$P_{cgw} = \frac{\sigma_{gw}}{R} \left[\cos \theta_{gwr} + \sqrt{\frac{\tan \alpha}{2} (\sin 2\theta_{gwr} - 2\theta_{gwr} - 2\alpha + \pi)} \right]. \quad (28)$$

For the displacement from configuration E to N, the energy balance equation $W = \Delta F$, with $N_{ow}^{fin} = 1$, $I_{go} = 1$ and $I_{gw} = 0$, may be written as

$$\begin{aligned} \frac{\sigma_{gw}}{r_{gw}} A_{ow}^{(2)} + \frac{\sigma_{go}}{r_{go}} (A_{go} - A_{ow}^{(2)}) &= L_{sow}^{(2)} \sigma_{gw} \cos \theta_{gwr} \\ &+ (L_{sgo} - L_{sow}^{(2)}) \sigma_{go} \cos \theta_{gor} + L_{fgo} \sigma_{go} - L_{fow}^{(2)} \sigma_{ow}, \end{aligned} \quad (29)$$

where the capillary pressures are expressed in terms of the radii of curvature by Eq. (4). The cross-sectional occupancy after invasion is shown in Fig. 3(b), and a view of the displacement in the direction along the tube is shown in Fig. 3(c). The gas-oil parameters are as follows:

$$r_{go} = \frac{\sigma_{go}}{\frac{\sigma_{gw}}{r_{gw}} - \frac{\sigma_{ow}}{r_{ow}}}, \quad (30)$$

$$A_{go} = \frac{R^2}{2 \tan \alpha} - \frac{r_{go} b_{go} \sin(\alpha + \beta_{go})}{2} + \frac{r_{go}^2 \beta_{go}}{2}, \quad (31)$$

$$L_{sgo} = \frac{R}{\tan \alpha} - b_{go}, \quad (32)$$

$$L_{fgo} = r_{go} \beta_{go}, \quad (33)$$

$$r_{go} \sin \beta_{go} = b_{go} \sin \alpha, \quad (34)$$

with β_{go} defined as

$$\beta_{go} = \frac{\pi}{2} - \alpha - \theta_{gor}. \quad (35)$$

Inserting Eqs. (30)–(35) into Eq. (29) then yields a polynomial

$$C_1 r_{go}^2 + C_2 r_{go} + C_3 = 0, \quad (36)$$

with the coefficients

$$C_1 = \frac{\sigma_{go}}{2} \left(\frac{\sin \beta_{go} \cos \theta_{gor}}{\sin \alpha} - \beta_{go} \right), \quad (37)$$

$$C_2 = \frac{\sigma_{ow} A_{ow}^{(2)}}{r_{ow}} - L_{sow}^{(2)} \sigma_{gw} \cos \theta_{gwr} - \left(\frac{R}{\tan \alpha} - L_{sow}^{(2)} \right) \sigma_{go} \cos \theta_{gor} + L_{fow}^{(2)} \sigma_{ow}, \quad (38)$$

and

$$C_3 = \sigma_{go} \frac{R^2}{2 \tan \alpha}. \quad (39)$$

The correct solution for r_{go} has to agree with a position b_{go} of the invading gas-oil AM located between the apex of the corner and the position $b_{ow}^{(2)}$. This condition may be formulated as

$$0 < r_{go} \leq \frac{b_{ow}^{(2)} \sin \alpha}{\sin \beta_{go}}. \quad (40)$$

The solution r_{go} that satisfies Eq. (40) is used to calculate P_{cgo} by Eq. (4). However, for some combinations of the capillary pressures it is possible that none of the solutions of Eq. (36) satisfy Eq. (40). In that case the gas-oil AM may either enter at position $b_{go} = b_{ow}^{(2)}$ with contact angle θ_{goh} , or, if $\theta_{goh} > \theta_{goa}$, the AM is instead invading at a position $b_{go} > b_{ow}^{(2)}$ with contact angle θ_{goa} . Piri and Blunt (2004) account for such capillary behavior, while we always assume the former case with gas-oil AMs entering position $b_{go} = b_{ow}^{(2)}$ if Eq. (40) is not satisfied. This simplification is reasonable since the latter case rarely occurs when contact angle hysteresis is assumed.

Thus, if Eq. (40) is not satisfied, the capillary entry pressures for the displacement to configuration N are calculated again using Eq. (29). Since the contact angle θ_{goh} of the gas-oil AM entering position $b_{go} = b_{ow}^{(2)}$ is unknown, the entry pressures have to be solved from an iterative procedure. In this case β_{go} is defined as

$$\beta_{go} = \frac{\pi}{2} - \alpha - \theta_{goh}. \quad (41)$$

Furthermore, $L_{sgo} = L_{sow}^{(2)}$, and hence the second term on the right-hand side of Eq. (29) vanishes. The capillary entry pressures are solved iteratively in the following manner: assume $r_{gw} = R$ as the initial value and calculate r_{go} , β_{go} , A_{go} and L_{fgo} from Eqs. (30), (31), (33), (34). A new value of r_{gw} is then calculated from Eq. (29). Finally, P_{cgo} and P_{cgw} are obtained from the converged values of r_{go} and r_{gw} , by Eq. (4).

For the displacement from configuration E to I Eqs. (13), (15) are applied with $N_{ow}^{fin} = 0$, $I_{go} = 0$, $I_{gw} = 1$. The gas-water AM invades at position $b_{gw} = b_{pd}$, implying that $L_{sgw} = L_{sow}^{(1)}$. Thus, the energy balance equation $W = \Delta F$, expressed in terms of radii of curvature by Eq. (4), is given by

$$\begin{aligned} \frac{\sigma_{gw}}{r_{gw}}(A_{gw} - A_{ow}^{(1)} + A_{ow}^{(2)}) + \frac{\sigma_{go}}{r_{go}}(A_{ow}^{(1)} - A_{ow}^{(2)}) = \\ L_{sow}^{(2)}\sigma_{gw}\cos\theta_{gwr} + (L_{sgw} - L_{sow}^{(2)})\sigma_{go}\cos\theta_{gor} \\ + L_{fgw}\sigma_{gw} - (L_{fow}^{(1)} + L_{fow}^{(2)})\sigma_{ow}, \end{aligned} \quad (42)$$

where

$$A_{gw} = \frac{R^2}{2\tan\alpha} - \frac{r_{gw}b_{pd}\sin(\alpha + \beta_{gw})}{2} + \frac{r_{gw}^2\beta_{gw}}{2}, \quad (43)$$

$$L_{sgw} = \frac{R}{\tan\alpha} - b_{pd}, \quad (44)$$

$$L_{fgw} = r_{gw}\beta_{gw}, \quad (45)$$

$$r_{gw}\sin\beta_{gw} = b_{pd}\sin\alpha, \quad (46)$$

with β_{gw} defined as

$$\beta_{gw} = \frac{\pi}{2} - \alpha - \theta_{gwh}. \quad (47)$$

The cross-sectional fluid occupancy after gas invasion is shown in Fig. 3(d), and the displacement in the direction along the tube is shown in Fig. 3(e). In this case the gas-water AMs are invading at an unknown hinging contact angle θ_{gwh} . The capillary entry pressures are solved iteratively in the following manner: assume $r_{gw} = R$ as the initial value and calculate r_{go} , A_{gw} , L_{sgw} , L_{fgw} and β_{gw} from Eqs. (30), (43)–(46). A new value of r_{gw} is obtained from Eq. (42). Finally, P_{cgo} and P_{cgw} are calculated from the converged values of r_{go} and r_{gw} .

The actual displacement occurring for different capillary pressures are determined from the three conditions for layer formation during invasion. If θ_{gwr} and θ_{gor} satisfy Eq. (12a), the following cases must be considered for configuration E:

- (i) The displacement is from configuration E to O if and only if the entry capillary pressures satisfy

$$P_{cgw}^{E \rightarrow O} < P_{cgw}^{col}, \quad P_{cgw}^{E \rightarrow O} < P_{cgw}^{E \rightarrow N} \quad \text{and} \quad P_{cgw}^{E \rightarrow O} < P_{cgw}^{E \rightarrow I}. \quad (48)$$

(ii) The displacement is from configuration E to N if and only if Eq. (48) is not met and the capillary entry pressures satisfy

$$P_{cgo}^{E \rightarrow N} < P_{cgo}^{col} \quad \text{and} \quad P_{cgo}^{E \rightarrow N} < P_{cgo}^{E \rightarrow I}. \quad (49)$$

(iii) The displacement is from E to I if and only if the capillary entry pressures do not satisfy Eqs. (48), (49).

If only θ_{gwr} satisfies Eq. (12a), formation of gas-oil AMs is not possible, and hence only the cases (i) and (iii) apply. Similarly, if only θ_{gor} satisfies Eq. (12a), water layers do not form, and hence only the cases (ii) and (iii) apply. Finally, if both θ_{gwr} and θ_{gor} does not satisfy Eq. (12a), only case (iii) applies as the only geometrically possible displacement is to configuration I.

Similar analysis of the entry capillary pressures is employed for the other oil-water configurations. An interesting consequence of using the most favorable entry pressure to determine the true displacement applies to mixed-wet tubes if AMs are absent at position b_{pd} before invasion. For example, gas invasion into configuration D is a displacement to configuration H or I. With $N_{ow}^{init} = 0$, $N_{ow}^{fin} = 1$, $I_{go} = 0$ and $I_{gw} = 1$ in Eqs. (13), (15) the energy balance $W = \Delta F$ becomes (Ma et al., 1996)

$$\frac{A_{gw}}{r_{gw}} = L_{fgw} + L_{sgw} \cos \theta_{gwr}, \quad (50)$$

where the gas-water parameters are given by Eqs. (43)–(47). For the displacement to configuration I P_{cgw} is calculated by iterations since the gas-water AM enters position b_{pd} at an unknown contact angle θ_{gwh} , while for the displacement to configuration H the resulting expression for P_{cgw} is given by Eq. (28). If the geometric conditions for the displacement to configuration H is fulfilled, i.e., if Eq. (12a) is met for θ_{gwr} and the corresponding entry pressure agree with a position $b_{gw} > b_{pd}$ of the gas-water AM, then the actual displacement is determined by comparing the entry pressures of the respective displacements to configurations I and H. Similar comparisons of the entry pressures are made for configurations B and G to determine if the actual displacement occurs with gas-water AMs entering position $b_{gw} = b_{pd}$ or $b_{gw} > b_{pd}$.

For oil invasion into cross-sections occupied by gas and water, the equivalents of Eqs. (13), (15) are given by

$$W = \{-P_{cgo}A_{go}I_{go} + P_{cow}A_{ow}I_{ow} + (P_{cgo} + P_{cow}) \sum_{k=N_{gw}^{fin}+1}^{N_{gw}^{init}} A_{gw}^{(k)}(-1)^k\} \delta x, \quad (51)$$

and

$$\begin{aligned} \Delta F = & \{(L_{fgo} - L_{sgo} \cos \theta_{goa})\sigma_{go}I_{go} + (L_{fow} + L_{sow} \cos \theta_{owr})\sigma_{ow}I_{ow} \\ & + (\sigma_{go} \cos \theta_{goa} + \sigma_{ow} \cos \theta_{owr}) \sum_{k=N_{gw}^{fin}+1}^{N_{gw}^{init}} L_{sgw}^{(k)} (-1)^k \\ & - \sigma_{gw} \sum_{k=N_{gw}^{fin}+1}^{N_{gw}^{init}} L_{fgw}^{(k)}\} \delta x, \end{aligned} \quad (52)$$

respectively. The cross-sectional parameters of the gas-water configurations H–L, $A_{gw}^{(k)}$, $L_{sgw}^{(k)}$ and $L_{fgw}^{(k)}$, are given by expressions similar to the corresponding oil-water parameters in configurations B, C and E–G. The capillary entry pressures and the associated displacements during oil invasion are derived correspondingly, except that displacements resulting in gas-oil AMs separating bulk oil from gas in layers are not allowed because of the assumed wetting sequences. Thus, $I_{go} = 0$ in Eqs. (51), (52).

5.2 Water into gas, oil and water

In the following we consider water invasion into cross-sections containing all three phases. In configuration O and Q the bulk phase is bounded by water layers, and water invasion is therefore a two-phase displacement with the associated entry capillary pressure given by simple two-phase expressions (e.g., Helland and Skjæveland, 2004a). As configuration P is already occupied by water in the bulk, the only possible configuration changes in this case are fluid-layer-collapse events. Thus, we restrict the analysis to cross-sections with oil layers surrounded by bulk gas and water in the corners, i.e., configuration M and N, as this is the only case where the three-phase entry capillary pressures are employed during waterflooding. The cross-sectional parameters of the oil-water AM in configuration M and N are given by Eqs. (16)–(20), with $b_{ow}^{(1)} = b_{pd}$ for configuration N. The parameters of the gas-oil AM are given by Eqs. (31)–(33), with β_{go} defined as in Eq. (41), and the position b_{go} expressed by

$$b_{go} = \frac{r_{go} \cos(\theta_{goh} + \alpha)}{\sin \alpha} \quad (53)$$

to account for the possibility of a hinging gas-oil contact angle before waterflooding.

Water invasion into configuration N is a displacement to configuration D, E or P, while water into configuration M results in either configuration G or D as additional AMs are not allowed to form, by assumption (ii), Section 4. If a reduced P_{cow} causes a change in configuration by an increase of the area of water in the corners, e.g., by a displacement from configuration M to H, then the capillary entry pressure and the associated displacement is updated for the new configuration during the simulations. In the following we omit descriptions of such configuration changes that may occur prior to piston-like invasion of water.

The gas-water capillary pressure at which the gas layer in configuration P collapses is (Piri and Blunt, 2005)

$$P_{cgw}^{col} = \begin{cases} P_{cgo} \frac{\sigma_{gw} \cos \theta_{gwa} + \sin \alpha}{\sigma_{go} \cos \theta_{goh} - \sin \alpha} & \text{if } \theta_{gwa} > \pi - \theta_{goh}, \\ P_{cgo} \frac{\sigma_{gw} \cos(\theta_{gwa} - \alpha)}{\sigma_{go} \cos(\theta_{goh} + \alpha)} & \text{if } \theta_{gwa} \leq \pi - \theta_{goh}, \end{cases} \quad (54)$$

and the oil-water capillary pressure at which the oil layers in configuration E and G collapses is (Helland and Skjæveland, 2004a)

$$P_{cow}^{col} = \frac{\sigma_{ow}(\xi^2 - 1)}{b_{ow}^{(1)}(\xi \cos \alpha + \sqrt{1 - \xi^2 \sin^2 \alpha})}, \quad (55)$$

where

$$\xi = \frac{\cos \theta_{owa}}{\sin \alpha} + 2. \quad (56)$$

We first consider the case when θ_{owa} and θ_{gwa} satisfy Eq. (12b) since then all assumed displacements are geometrically possible. The capillary entry pressure for the displacement from configuration N to P is given by the simple two-phase expression

$$P_{cgw} = \frac{\sigma}{R} \left[\cos \theta_{gwa} - \sqrt{\frac{\tan \alpha}{2} (-\sin 2\theta_{gwa} + 2\theta_{gwa} - 2\alpha - \pi)} \right]. \quad (57)$$

For the displacements to configuration E or G the energy balance equation yields

$$\begin{aligned} \frac{\sigma_{gw}}{r_{gw}} A_{go} + \frac{\sigma_{ow}}{r_{ow}} (A_{ow}^{(2)} - A_{go}) &= L_{sgo} \sigma_{gw} \cos \theta_{gwa} \\ &+ (L_{sow}^{(2)} - L_{sgo}) \sigma_{ow} \cos \theta_{owa} + L_{fgo} \sigma_{go} - L_{fow}^{(2)} \sigma_{ow}, \end{aligned} \quad (58)$$

where the capillary pressures are expressed in terms of the radii of curvature by Eq. (4). The cross-sectional parameters of the oil-water AM that forms in the displacement is given by Eqs. (22)–(24), where $b_{ow}^{(2)}$ is obtained from Eq. (11) with $\theta_{ow} = \theta_{owa}$, and

$$\beta_{ow}^{(2)} = \frac{\pi}{2} + \alpha - \theta_{owa}. \quad (59)$$

Since the invading oil-water AM is not assumed to be hinging, Eq. (58) is formulated as a polynomial which can be solved for r_{ow} when r_{gw} is eliminated from the expressions by Eq. (6):

$$C_1 r_{ow}^2 + C_2 r_{ow} + C_3 = 0, \quad (60)$$

where the coefficients are given by

$$C_1 = \frac{\sigma_{ow}}{2} \left(\frac{\sin \beta_{ow}^{(2)} \cos \theta_{owa}}{\sin \alpha} + \beta_{ow}^{(2)} \right), \quad (61)$$

$$C_2 = \frac{\sigma_{go} A_{go}}{r_{go}} - L_{sgo} \sigma_{gw} \cos \theta_{gwa} - \left(\frac{R}{\tan \alpha} - L_{sgo} \right) \sigma_{ow} \cos \theta_{owa} - L_{fgo} \sigma_{go}, \quad (62)$$

and

$$C_3 = \sigma_{ow} \frac{R^2}{2 \tan \alpha}. \quad (63)$$

The solution of Eq. (60) has to agree with a position $b_{ow}^{(2)}$ of the invading oil-water AM located between the apex of the corner and the position b_{go} of the gas-oil AM. Thus, the solution r_{ow} that satisfies

$$\frac{b_{go} \sin \alpha}{\sin \beta_{ow}^{(2)}} \leq r_{ow} < 0 \quad (64)$$

is used to calculate P_{cow} from Eq. (4). However, for some combinations of the capillary pressures it is possible that none of the solutions of Eq. (60) satisfy Eq. (64). In that case, the oil-water AM is assumed to invade at position $b_{ow}^{(2)} = b_{go}$ with a hinging contact angle $\theta_{owh}^{(2)}$ which is now related to $\beta_{ow}^{(2)}$ by Eq. (21). The capillary entry pressures are calculated iteratively from Eq. (58) and Eqs. (21)–(25) as described in Section 5.1.

For the displacements from configuration M or N to D the energy balance yields

$$\begin{aligned} \frac{\sigma_{gw}}{r_{gw}} A_{go} + \frac{\sigma_{ow}}{r_{ow}} (A_{ow}^{(1)} - A_{go}) &= L_{sgo} \sigma_{gw} \cos \theta_{gwa} \\ + (L_{sow}^{(1)} - L_{sgo}) \sigma_{ow} \cos \theta_{owa} &+ L_{fgo} \sigma_{go} + L_{fow}^{(1)} \sigma_{ow}. \end{aligned} \quad (65)$$

Eq. (65) and Eqs. (6), (16)–(20) are solved iteratively for r_{ow} , and the capillary entry pressures are calculated from Eq. (4) using the converged values of r_{ow} and r_{gw} .

The actual displacements occurring are determined next. If θ_{gwa} and θ_{owa} satisfy Eq. (12b), the following cases must be considered for configuration N:

- (i) The displacement is from configuration N to P if and only if the capillary entry pressures satisfy

$$P_{cgw}^{N \rightarrow P} > P_{cgw}^{col}, \quad P_{cgw}^{N \rightarrow P} > P_{cgw}^{N \rightarrow E} \quad \text{and} \quad P_{cgw}^{N \rightarrow P} > P_{cgw}^{N \rightarrow D}. \quad (66)$$

- (ii) The displacement is from configuration N to E if and only if Eq. (66) is not met and the capillary entry pressures satisfy

$$P_{cow}^{N \rightarrow E} > P_{cow}^{col} \quad \text{and} \quad P_{cow}^{N \rightarrow E} > P_{cow}^{N \rightarrow D}. \quad (67)$$

- (iii) The displacement is from N to D if and only if the capillary entry pressures do not satisfy Eqs. (66), (67).

If only θ_{gwa} satisfies Eq. (12b), formation of new oil-water AMs is not possible, and hence only the cases (i) and (iii) apply. Similarly, if only θ_{owa} satisfies Eq. (12b),

gas layers do not form, and hence only the cases (ii) and (iii) apply. Finally, if both θ_{owa} and θ_{gwa} do not satisfy Eq. (12b), only case (iii) applies as the only geometrically possible displacement is to configuration D. The analysis of configuration M is similar for the different contact angle combinations, except that formation of additional AMs are not allowed, as commented earlier. Thus, only the cases (ii) and (iii) apply to determine the displacements from configuration M in waterflooding.

6 Numerical experiments

We have performed several simulations of gas and water invasion processes to study the effect of a variable saturation history on the three-phase entry pressures and to analyze the saturation dependencies of the capillary pressures. The simulations are conducted on a bundle of 2000 tubes. The inscribed radii of the triangular tubes are calculated from Eq. (7) assuming $R_{\min} = 1\mu\text{m}$, $R_{\max} = 100\mu\text{m}$, $R_{\text{ch}} = 20\mu\text{m}$ and $\eta = 2$. We consider a fluid system with the interfacial tensions $\sigma_{go} = 0.015\text{ N/m}$, $\sigma_{ow} = 0.045\text{ N/m}$ and $\sigma_{gw} = 0.055\text{ N/m}$, representing realistic values for a system of water, crude oil and natural gas (Whitson and Brulè, 2000). Three different wettability conditions are modelled, and the contact angles for each case are presented in Table 3. Advancing and receding gas-oil and gas-water contact angles are calculated from Eqs. (1), (2), respectively, from the specified values of θ_{owr} and θ_{owa} . The advancing contact angles of case 1 indicate strongly oil-wet conditions and the receding contact angles indicate weakly oil-wet conditions. Case 2 always represents strongly oil-wet conditions, whereas the contact angle hysteresis of case 3 suggests weakly oil-wet conditions during waterflooding and water-wet conditions during gas injection.

Although the model allows for any two-phase oil-water saturation history starting with primary drainage, we have decided to introduce the gas phase after the first imbibition in all simulations. This sequence of processes may occur in reservoirs where gas is injected to increase oil recovery by pressure maintenance. The two-phase saturation history is varied by terminating primary drainage at several values of P_{cow}^{\max} , and by simulating gas invasion processes at different P_{cow} after imbibition. Waterflooding processes are simulated from different capillary levels on selected gas invasion trajectories.

Case	θ_{pd}	θ_{owa}	θ_{owr}	θ_{gwa}	θ_{gwr}	θ_{goa}	θ_{gor}
1	0°	180°	100°	123.1°	84.7°	30.4°	0°
2	0°	180°	160°	123.1°	119.9°	8.1°	0°
3	0°	100°	80°	84.7°	68.8°	36.5°	30.4°

Table 3

Contact angles for the three different wetting conditions.

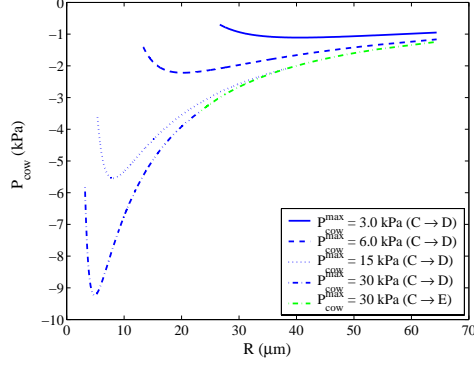


Figure 4. Two-phase capillary entry pressures for imbibition as a function of pore size for several P_{cow}^{\max} and contact angles of case 1 and 2.

6.1 Sensitivity analysis of three-phase capillary entry pressure

Capillary entry pressures are studied for piston-like displacements in gas invasion and the following water invasion. For contact angles of case 1 and 2, configuration E occurs frequently during imbibition, while configuration N may occur in the subsequent gas injection. For gas invasion into configuration E, we investigate if variations of P_{cow}^{\max} (corresponding to variations of b_{pd} by Eq. (8)) and P_{cow} (corresponding to variations of $b_{ow}^{(2)}$ by Eq. (25)) are sensitive to P_{cgw} for the actual displacements occurring. Similarly, for water into configuration N, we explore if P_{cgw} is sensitive to variations of P_{cow}^{\max} and P_{cgo} (corresponding to variations of b_{go} by Eq. (53)).

We have previously found that the oil-water capillary entry pressure is sensitive to P_{cow}^{\max} for displacements from configuration C to D when $\theta_{owa} > \frac{\pi}{2}$ (Helland and Skjæveland, 2004a). This effect is demonstrated in Fig. 4. The distance b_{pd} decreases according to an increased P_{cow}^{\max} by Eq. (8), resulting in lower entry pressures. The smaller tubes are more affected by the hinging oil-water AMs in the corners than the larger tubes since b_{pd} does not depend on pore size. Thus, the peculiar invasion order manifested by Fig. 4 depends on both pore size and fraction of water-wet surface. However, the entry pressure for the limiting displacement from configuration C to E does not depend on P_{cow}^{\max} as the displacement is unaffected by the water in the corners.

Results for case 1 with variation of P_{cow}^{\max} and other parameters fixed are shown in Fig. 5. The displacements from configuration E to I exhibit a slight increase of P_{cgw} as the level of P_{cow}^{\max} is increased. A more pronounced dependence of P_{cgw} is observed when water into configuration N results in configuration D. In this case P_{cgw} decreases with increasing P_{cow}^{\max} , as shown in Fig. 5(b). Thus, an increased water content in the corners tend to increase the entry pressure. This is similar to the two-phase behavior presented in Fig. 4. The bottom curve in Fig. 5(b) represents the limiting displacement from configuration N to E when P_{cgw} evidently does

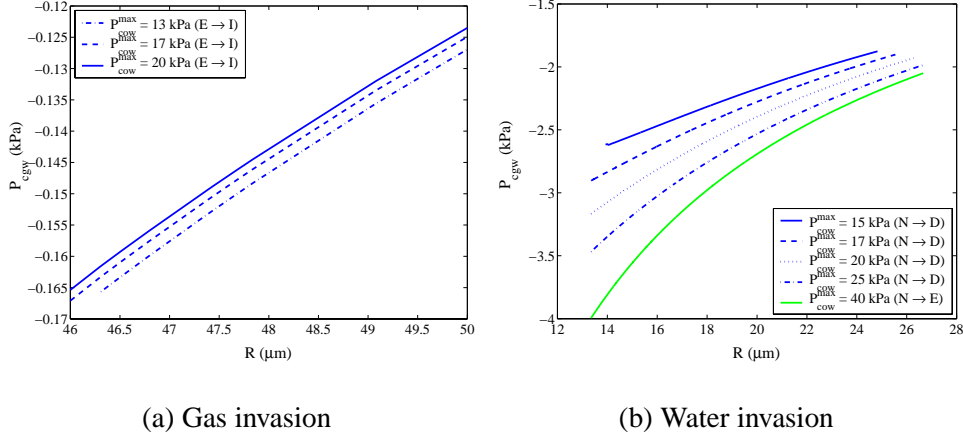
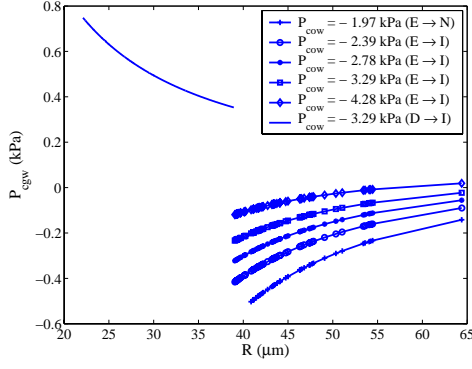


Figure 5. Capillary entry pressures as a function of pore size with different P_{cow}^{\max} for contact angles of case 1. (a) P_{cgw} for displacements E to I with $P_{cow} = -3.0$ kPa fixed. (b) P_{cgw} for displacements N to D and E with $P_{cgo} = 2.0$ kPa fixed. Gas was injected at $P_{cow} = -3.0$ kPa.

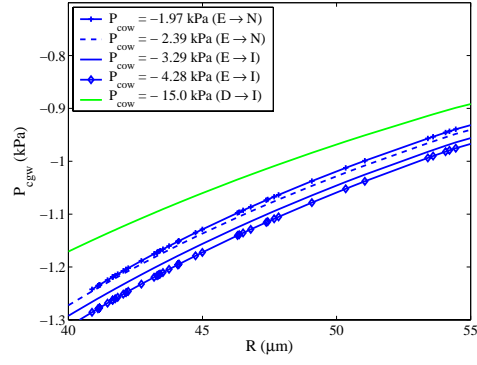
not depend on P_{cow}^{\max} anymore. Corresponding experiments performed with contact angles of case 2 show the same sensitivity.

The effects of a variable P_{cow} in displacements resulting from gas invasion into configuration E is investigated while P_{cow}^{\max} is unchanged. The results for contact angles of case 1 and 2 are shown in Fig. 6(a), (b). The variations of P_{cow} presented in Fig. 6(a) for case 1 contact angles are more sensitive to P_{cgw} than the variations of P_{cow}^{\max} plotted in Fig. 5(a). In displacements from configuration E to I and N, P_{cgw} is negative and decreasing according to pore size even though $\theta_{gor} < \frac{\pi}{2}$ and $\theta_{gwr} < \frac{\pi}{2}$. This is because the area of oil in layers is constant for all pore sizes, and hence the oil layers affect the entry pressure increasingly as pore size decreases. Since the distance $b_{ow}^{(2)}$ decreases with P_{cow} , it is expected that P_{cgw} increases as P_{cow} decreases. Eventually the limiting level of P_{cow} is approached, corresponding to displacements from configuration D to I where the oil layers have collapsed before invasion. This latter displacement, which is independent of P_{cow} since oil is absent, also occurs in smaller pore sizes where configuration E has not formed, as shown in Fig. 6(a). In this case P_{cgw} is positive and monotonic increasing as pore size decreases. The experiment with contact angles of case 2 presented in Fig. 6(b) exhibits the opposite behavior since $\theta_{gwr} > \frac{\pi}{2}$. In this case P_{cgw} decreases according to P_{cow} , and thus for a smaller distance $b_{ow}^{(2)}$ the bulk gas-water displacement occurring with contact angle θ_{gwr} affects P_{cgw} to a greater extent. However, in the limiting displacement from configuration D to I, the gas-water AMs enter position $b_{gw} = b_{pd}$ while oil layers are absent, resulting in a higher level of P_{cgw} , as shown in Fig. 6(b).

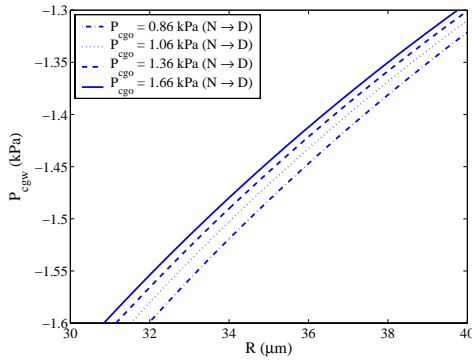
The effects of a variable P_{cgo} on the entry pressures for water invasion into configuration N is investigated while the capillary pressures after primary drainage and



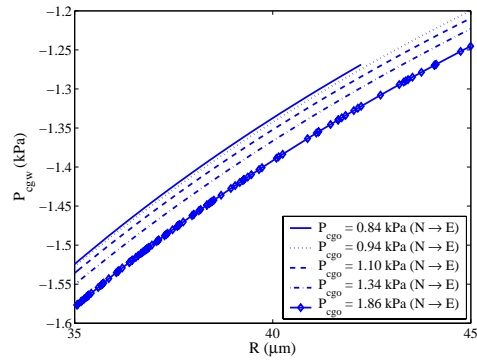
(a) Gas invasion, case 1



(b) Gas invasion, case 2



(c) Water invasion, case 1



(d) Water invasion, case 2

Figure 6. Capillary entry pressures as a function of pore size with P_{cow}^{\max} constant. (a), (b) Effect of P_{cow} on P_{cgw} for displacements E to I and N with $P_{cow}^{\max} = 15$ kPa. (c) Effect of P_{cgo} on P_{cgw} for displacement N to D with $P_{cow}^{\max} = 15$ kPa. Gas was injected at $P_{cow} = -1.97$ kPa. (d) Effect of P_{cgo} on P_{cgw} for displacements N to E with $P_{cow}^{\max} = 150$ kPa. Gas was injected at $P_{cow} = -3.0$ kPa.

imbibition are fixed. Since the advancing contact angles of case 1 and 2 are equal, the same behavior occurs in water invasion for both cases. Results are presented in Fig. 6(c), (d) for two different P_{cow}^{\max} values. The displacement to configuration D is favorable for small P_{cow}^{\max} , and P_{cgw} increases according to P_{cgo} in this case. For a much larger P_{cow}^{\max} , the displacement to configuration E occurs, with P_{cgw} decreasing as P_{cgo} is increased. However, the variations of P_{cgw} shown in Fig. 6(c) are smaller than the variations occurring when P_{cow}^{\max} is changed, as shown in Fig. 5(b). Thus, for the particular sequence of processes investigated here using the specified interfacial tensions and contact angles of case 1 or 2, we find that P_{cgw} is more sensitive to the location of the oil-water AM than the gas-oil AM for the range of capillary pressures where the displacements from configuration N to D occur.

6.2 Saturation dependencies

The capillary pressure vs. saturation relationships computed from the bundle of triangular tubes are compared with the results from a bundle of cylindrical tubes, using the constraint that the total cross-sectional area of all tubes, A_p , and the capillary pressure curves for primary drainage are identical in both models. This enables us to study the effect of pore geometry and contact angle hysteresis on the subsequent invasion processes. van Dijke et al. (2001a,b) analyzed the saturation dependencies of three-phase capillary pressures and relative permeabilities for mixed-wet conditions without contact angle hysteresis using a bundle of cylindrical tubes. They identified three regions in the saturation space where the capillary pressures have different saturation dependencies. In each region one phase acts as “intermediate-wetting” in the sense that only the capillary pressure between the other two phases depends on more than one saturation. The regions remain unchanged for all invasion processes, since there exists a unique relation between saturation and pore occupancy. This is certainly not true if contact angle hysteresis is assumed since different pore occupancies may occur for the same saturations. Thus, the location, size, and existence of these regions depend in general on the invasion processes and the saturation history for a given set of interfacial tensions and contact angles. In accordance with van Dijke et al. (2001a,b), we take oil as intermediate-wetting phase in region I, gas as intermediate-wetting in region II, and water as intermediate-wetting in region III.

The bundle of cylindrical tubes is made comparable to the bundle of triangular tubes in the following manner: a set of primary drainage data $(P_{cow}, S_w)_i, i = 1, \dots, m + 1$, calculated from a model of m triangular tubes, is used to calculate m cylindrical pore sizes R_i from the Young-Laplace equation:

$$R_i = \frac{2\sigma_{ow} \cos \theta_{pd}}{P_{cow,i}}, \quad i = 1, \dots, m. \quad (68)$$

The frequencies of the cylindrical pore sizes, f_i , are calculated from the relation

$$f_i \pi R_i^2 = -\Delta S_{w,i} A_p, \quad i = 1, \dots, m, \quad (69)$$

where the data are organized in the order of decreasing water saturation, and $\Delta S_{w,i} = S_{w,i+1} - S_{w,i}$. The same contact angles and interfacial tensions are employed for the respective geometries. The simulation procedures are similar for both models, except that in the bundle-of-cylindrical-tubes model the cross-sectional areas are multiplied by the corresponding pore-size frequencies in the saturation calculations. Only four cross-sectional fluid configurations apply to the cylindrical geometry, of which one is equivalent to configuration A, representing cross-sections that always have been occupied by water. The three other configurations represent cross-sections occupied by gas, oil and water in cases where the wettability has been allowed to change. Consistently with the assumptions for the triangular con-

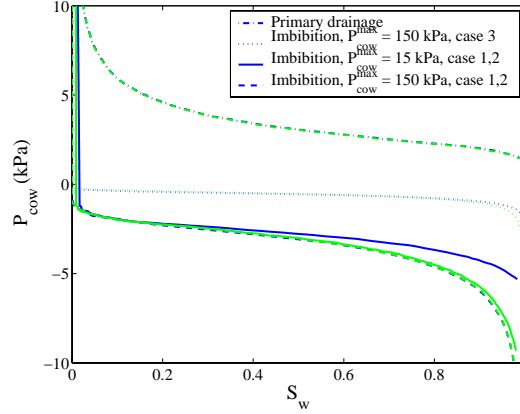


Figure 7. Capillary pressure curves for primary drainage and imbibition for the triangular (in blue) and cylindrical (in green) geometries.

figurations, we do not allow gas to invade the waterfilled cylindrical cross-sections where oil has never been.

Two-phase capillary pressure curves are shown in Fig. 7. The imbibition curves from the two models are in good agreement for high values of P_{cow}^{\max} , while pronounced differences can occur if P_{cow}^{\max} is decreased. This is caused by the capillary behavior in the triangular tubes demonstrated in Fig. 4. In the simulations with contact angles of case 1, primary drainage is terminated when $P_{cow}^{\max} = 15$ kPa. At this capillary level some of the smallest pore sizes remain waterfilled. During imbibition of the bundle of triangular tubes, the configurations may be arranged as A–D–C–D–E in order of increasing pore size at a certain capillary level. The imbibition process for the bundle of cylindrical tubes is much simpler. Starting with the largest pore size, water invades successively smaller pores. Thus, the discrepancies observed in the shape of the two imbibition curves in Fig. 7 is explained by different entry pressures, which results in different invasion orders of the pore sizes in the two models.

Displacement paths for the subsequent gas invasion are shown in Fig. 8(a). The simulations by both models are generated from equal initial saturations. This implies that the corresponding trajectories calculated by the two bundles represent oil-water “iso-caps” (capillary pressure iso-lines) at different levels of P_{cow} since the imbibition curve for the triangular and cylindrical geometry generally differs, as shown in Fig. 7. In the bundle-of-triangular-tubes-model, the displacements are in general from configuration C to I and N in the smaller pores, from configuration D to I in the medium-sized pores, and from configuration E to I and N in the larger pores. A deviation from this scenario occurs for the gas invasion at $S_w = 0.1$, where configuration D has not yet formed, and for gas invasion at $S_w = 0.9$, where the displacement D to I occurs in some of the smallest pores as well. The trajectories generated from the bundle of cylindrical tubes show that gas first invades most of the pores occupied by oil, representing a large region in the saturation space where P_{cow} depends only on S_w , followed by simultaneous invasion into pores occupied

by oil and water, representing a small region II where P_{cow} depends on two saturations. The corresponding results generated from the bundle of triangular tubes agree fairly well, except that the region where P_{cow} depends on two saturations is larger. This can be explained by different entry pressure in the models, as shown in Fig. 9(a) for gas invasion at $S_w = 0.1$ where the deviation in region II is conspicuous. Since the gas-oil capillary pressure required for gas to enter configuration E is lower than for corresponding gas-water displacements in the cylindrical tubes, larger oil-filled pore sizes are invaded simultaneously, resulting in a larger region for the triangular geometry where P_{cow} depends on two saturations. The displacements E to I and N occur at entry pressures increasing with pore size, as opposed to similar displacements in cylindrical tubes. This effect may also yield further deviations in region II. However, smaller deviations are expected for gas injections at larger water saturations since P_{cgw} for gas into configuration E increases as P_{cow} decreases, as demonstrated in Fig. 6(a).

The following waterfloods are initiated from various saturations on the gas invasion path starting at $S_w = 0.1$. Since the gas invasion paths for the two models differ slightly, waterfloods for the triangular tubes are generated in such a way that the displacement paths meet the initial point on the corresponding trajectories for the cylindrical tubes, as shown in Fig. 8(b). The displacement paths calculated from the two bundles represent gas-oil iso-caps at different levels of P_{cgo} since the capillary pressure in gas invasion for the two geometries generally differs. In all the waterfloods of the triangular tubes the displacements are from configuration C to D in the smaller tubes and from configuration N to D in the larger tubes. The oil-water capillary pressure for these displacements are plotted in Fig. 9(b) as a function of pore size. The capillary behavior in the displacement C to D is equivalent to the behavior shown in Fig. 4. Clearly, gas first invades all pores occupied by bulk oil, except for the waterfloods initiated from the two lower P_{cgo} values, where the displacements C to D occurs simultaneously in some of the smaller pores. Moreover, in the displacements N to D, oil in layers are displaced in addition to the bulk gas, which further explains why the trajectories does not follow the lines of constant oil saturations exactly. However, these effects are absent in the cylindrical tubes, and thus the trajectories traces lines of constant oil saturations, implying that P_{cgo} depends only on S_o .

Because of contact angle hysteresis, different saturation dependencies may occur in the different invasion processes. To investigate this, we calculate iso-caps for the remaining two capillary pressures from the gas and water invasion data, by employing the `contour` function in MATLAB[†]. This function uses an interpolation method to calculate iso-lines, and thus small oscillations may occur in the results due to possible abrupt changes in the directions of the displacement paths. Nevertheless, general trends can be read from the results, and consequently regions of different saturation dependencies can be detected. Lines of constant P_{cgo} and P_{cgw} for gas in-

[†] MATLAB is a registered trademark of TheMathWorks Inc.

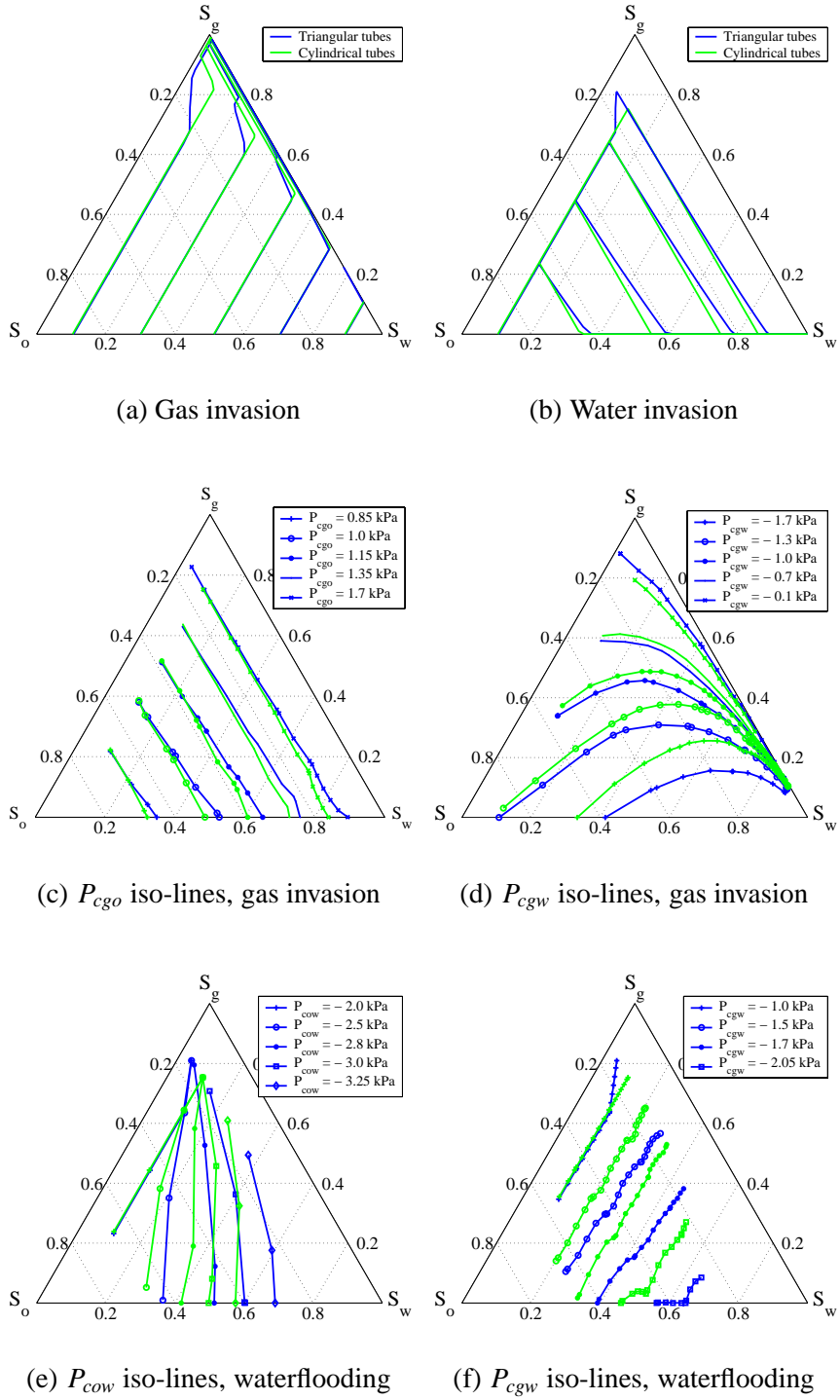


Figure 8. Results for triangular tubes (in blue) and cylindrical tubes (in green) using contact angles of case 1. (a), (b) Displacement paths for gas and water invasion. (c), (d) P_{cgo} and P_{cgw} iso-lines calculated for gas invasion. (e), (f) P_{cow} and P_{cgw} iso-lines calculated for water invasion.

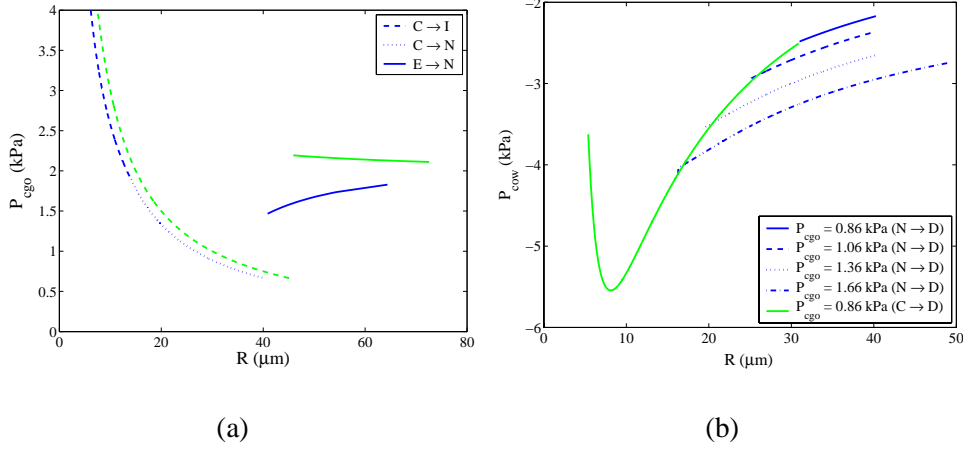


Figure 9. Capillary pressure as a function of pore size with case 1 parameters. (a) P_{cgo} for the displacements occurring in the gas invasion starting at $S_v = 0.1$. Triangular tubes (in blue) are compared with cylindrical tubes (in green). (b) P_{cow} for displacements occurring in the triangular tubes during the waterfloods.

vasion are shown in Fig. 8(c), (d) providing additional evidence of the existence of region I in most of the saturation space for the cylindrical tubes. The results for the triangular tubes exhibit the same general trends, and thus P_{cow} is a function of S_w , P_{cgo} is a function of S_o , while P_{cgw} depends on two saturations. However, because of the possibility of simultaneous displacement of the phases occupying a triangular cross-section, these dependencies are only approximate, although the deviations caused by displacement of fluid layers may not be visible in the plots. Other reasons why P_{cgo} is not unique with respect to S_o are addressed when the simulation results for contact angles of case 3 are discussed. The level of P_{cgo} agrees fairly well for both models, while the level of P_{cgw} is generally higher for the triangular tubes. This is explained by the increased difference of imbibition capillary pressure at large S_w , resulting in different levels of P_{cgw} by Eq. (5). Lines of constant P_{cow} and P_{cgw} during the waterfloods are shown in Fig. 8(e), (f). In this case both P_{cow} and P_{cgw} are higher for the triangular tubes. This is explained by the effect of water in the corners in displacements from C to D and N to D, as demonstrated in Fig. 4 and Fig. 5(b), respectively. During waterflooding of the cylindrical tubes, region II occurs, and thus P_{cow} has become a function of two saturations, while P_{cgw} depends only on S_w , and P_{cgo} depends only on S_o . As in gas invasion, these dependencies are only approximate for the triangular tubes although the results display the same qualitative trends. The different saturation dependencies appearing in the gas and water invasion processes are caused by significant hysteresis between receding and advancing oil-water and gas-water contact angles.

We have shown that the capillary entry pressures, and thereby the level of capillary pressure, may be strongly affected by the value of P_{cow}^{\max} . To investigate if a changed reversal point after primary drainage can result in different saturation dependencies as well, we simulate the gas and water invasion processes with contact angles of

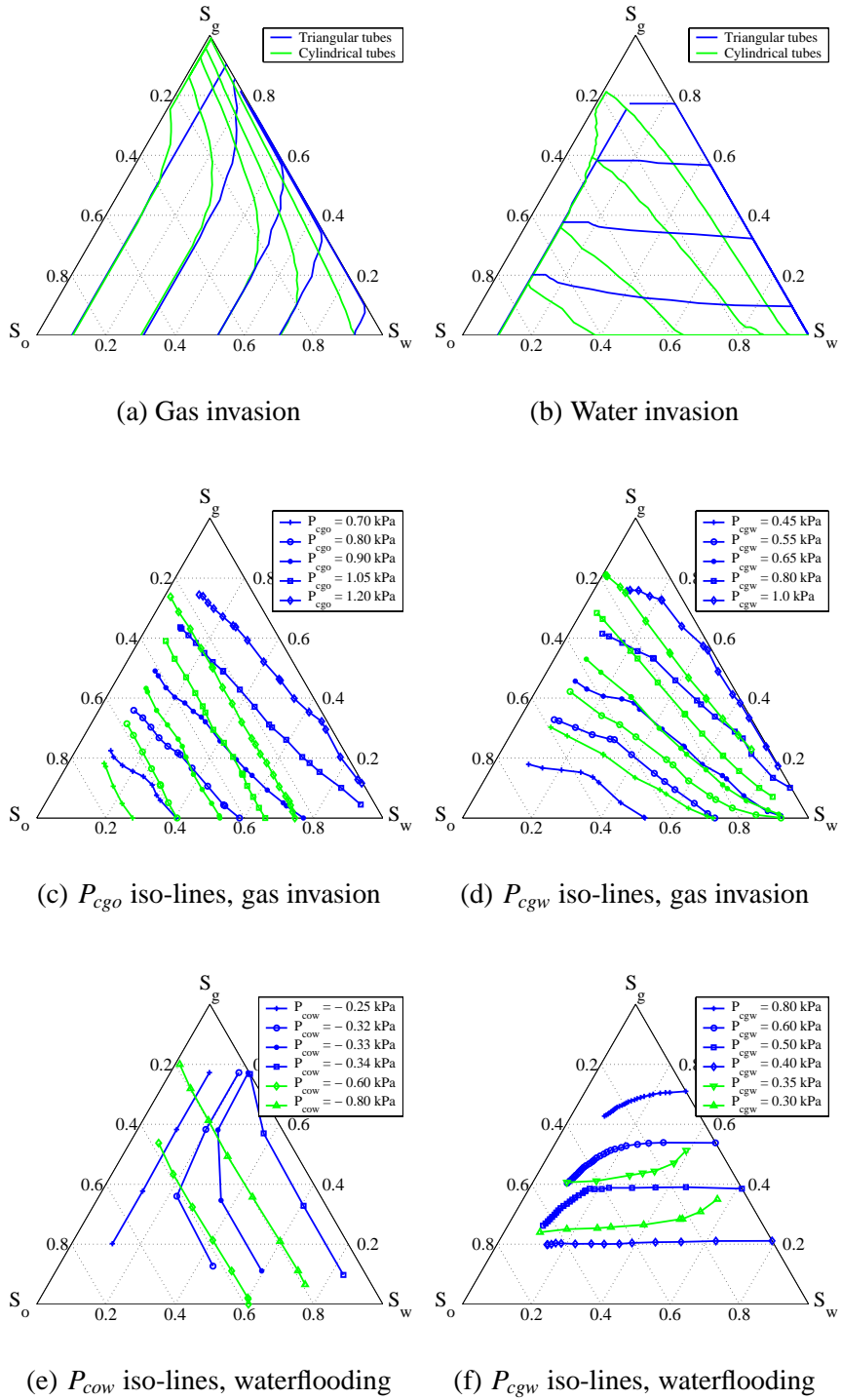


Figure 10. Results for triangular tubes (in blue) and cylindrical tubes (in green) with contact angles of case 3 and $P_{cow}^{max} = 15$ kPa. (a), (b) Displacement paths for gas and water invasion. (c), (d) P_{cgo} and P_{cgw} iso-lines calculated for gas invasion. (e), (f) P_{cow} and P_{cgw} iso-lines calculated for water invasion.

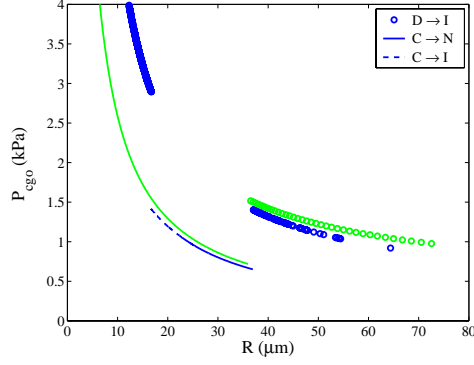


Figure 11. Gas-oil capillary pressure as a function of pore size for gas invasion with contact angles of case 3 and $P_{cow}^{\max} = 15$ kPa. Results for triangular tubes (in blue) and cylindrical tubes (in green) are compared.

case 2 and 3 for two very different values of P_{cow}^{\max} . The gas invasion trajectories for contact angles of case 3 with $P_{cow}^{\max} = 15$ kPa are shown in Fig. 10(a). During gas injection, the displacements are from configuration D to I in the smaller pores, from C to I and N in the medium-sized pores, and from D to I in a few large pores. The arrangement of displacements is different in the model of cylindrical tubes where gas invasion into waterfilled pores exclusively occurs in the large pores and invasion into oil occurs in the smaller pores. This feature causes large differences in the displacement paths at small S_o for the two models. Fig. 11 shows a comparison of P_{cgo} for the displacements occurring in the bundles when gas is injected at $S_w = 0.3$. In the range of P_{cgo} where simultaneous invasion into medium-sized oilfilled pores and large waterfilled pores occurs, the water saturation exhibits a more pronounced decrease for the cylindrical tubes, as shown in Fig. 10(a). This is caused by the different water distributions in the bundles, and thus the contribution of S_w from the large cylindrical pore sizes is larger than from the corresponding triangular tubes. At higher P_{cgo} , gas displaces bulk water in the triangular tubes while gas displaces oil in the cylindrical tubes, as demonstrated by Fig. 11.

The gas invasion trajectories and the calculated gas-oil and gas-water iso-caps, presented in Fig. 10(a), (c), (d), respectively, reveal that region I occurs for the cylindrical tubes at high S_o , and thus P_{cgo} depends on two saturations, while P_{cgo} is a function of only S_o . However, the corresponding results from the triangular tubes show that both P_{cgo} and P_{cgo} depend strongly on two saturations. The different saturation dependencies of P_{cgo} are caused by different water distributions in the bundles. This is illustrated in Fig. 12(a), (b), where the pore occupancies in the bundles are indicated for gas injection at two different initial water saturations S_{w1} and S_{w2} . The corresponding largest oilfilled pores prior to gas invasion is R_1 and R_2 . In the bundle of cylindrical tubes, gas invades successively smaller oilfilled pores, and thus R_2 is invaded at the same oil saturation in both cases, implying that $P_{cgo2} = P_{cgo}(R_2)$ corresponds to a unique oil saturation S_{o2} . Thus, P_{cgo} depends on only the oil saturation, which is in agreement with similar analysis made by van Dijke et al. (2001a,b). However, this dependency is violated for the triangular ge-

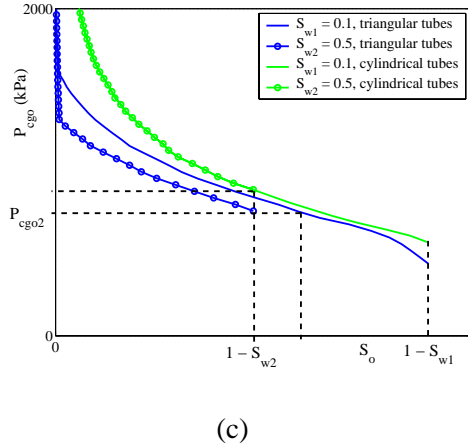
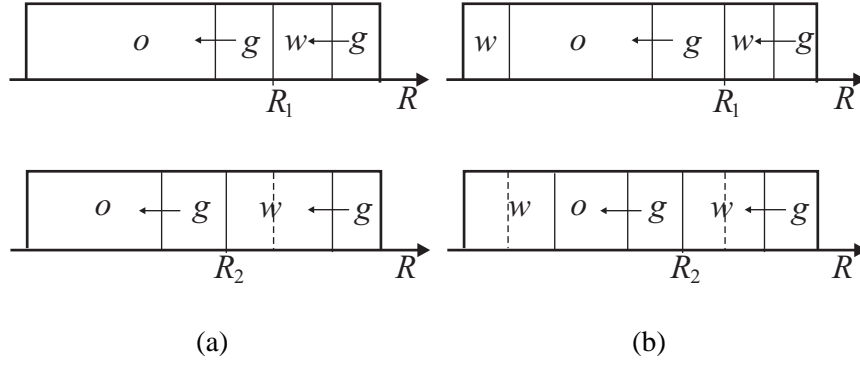


Figure 12. Sketches of the bulk pore occupancies during gas invasion with contact angles of case 3 and $P_{cow}^{\max} = 15$ kPa. Gas is injected at initial water saturations S_{w1} and S_{w2} , and the largest oilfilled pore size before gas invasion is R_1 and R_2 in the two cases. For clarity, waterfilled pores of configuration A are not shown. (a) Cylindrical tubes. (b) Triangular tubes. (c) Corresponding $P_{cgo} - S_o$ curves.

ometry since water also invades the smaller pore sizes in the preceding imbibition, as depicted in Fig. 12(b). Consequently, gas invades pore size R_2 at different oil saturations in the two gas invasion processes, implying that the oil saturation is not unique with respect to P_{cgo2} , as shown in Fig. 12(c). If P_{cow}^{\max} is reduced, water may only invade the smaller triangular tubes during imbibition, by Fig. 4. In that case, a similar reasoning based on pore occupancies implies that P_{cgo} becomes a function of only S_g . At smaller oil saturations, gas starts to invade the large waterfilled pores in order of decreasing pore size, as illustrated in Fig. 12(a), (b). This can occur at different saturation combinations in both models, and thus P_{cow} and P_{cgw} are functions of two saturations in the bundle of cylindrical tubes, while all *three* capillary pressures are functions of two saturations in the triangular tubes, as shown in Fig. 10(a), (c), (d). Such regions where more than one capillary pressure depends on two saturations occurs because of contact angle hysteresis and were therefore not identified by van Dijke et al. (2001a,b).

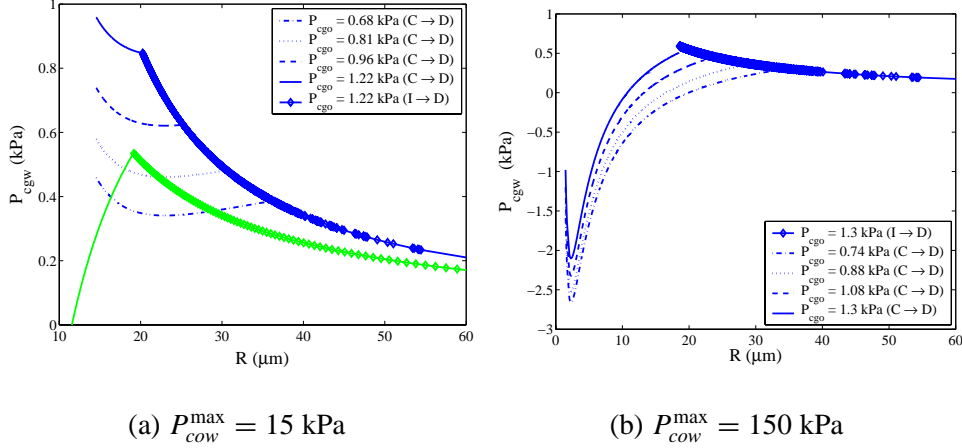


Figure 13. Gas-water capillary pressure as a function of pore size for the waterfloods with contact angles of case 3. (a) Results for triangular tubes (in blue) and cylindrical tubes (in green) are compared when $P_{cow}^{\max} = 15 \text{ kPa}$. (b) Results for triangular tubes when $P_{cow}^{\max} = 150 \text{ kPa}$.

The displacement paths for the subsequent waterfloods, presented in Fig. 10(b), exhibit conspicuous differences between the two models. The configurations for the triangular tubes are in general arranged as A–D–C–N–D in order of increasing pore size at the different stages where the preceding gas invasion was terminated. The oil layers in configuration N collapse at early stages of the waterfloods because of increased water content in the corners. This results in sudden increases of the gas and water saturations before the piston-like displacements take place, as shown for the waterflood originating from the highest gas saturation in Fig. 10(b). Thus, the displacements are from configuration N to I to D and from C to D. The differences in the behavior of P_{cgw} during waterflooding of the two bundle models are illustrated in Fig. 13(a). Clearly, the deviations are caused by the displacements from configuration C to D.

Fig. 10(b), (e), (f) reveal that region III occurs for the cylindrical tubes during waterflooding, and thus P_{cgo} depends on two saturations, while P_{cow} is a function of only S_o , and P_{cgw} is a function of only S_g . However, the dependency of P_{cgw} is violated for small oil saturations since two of the waterfloods are originating from smaller water saturations, and thus gas has started to invade the largest pores before the preceding gas injection was terminated. This is illustrated by the pore occupancies shown in Fig. 14(a). The results for the triangular tubes exhibit two regions where the capillary pressure have different saturation dependencies. The pore occupancies at early stages of the waterfloods, where water only invades configuration C, are shown in Fig. 14(b) (top). The water saturation is more or less constant in the preceding gas injection, implying that P_{cow} is a function of S_w in this region, while P_{cgw} is a function of two saturations. These dependencies are further demonstrated by Fig. 10(e), where the P_{cow} iso-lines track constant water saturations, while the iso-lines of P_{cgw} are curved, as shown in Fig. 10(f). Moreover, P_{cgo} is a function of

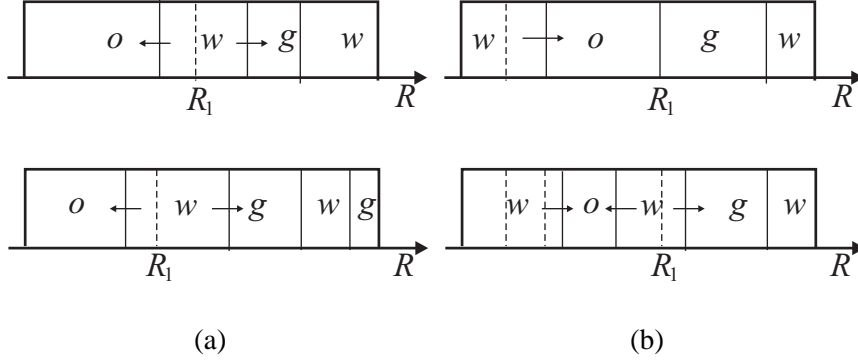


Figure 14. Sketches of the bulk pore occupancies during waterflooding for contact angles of case 3 and $P_{cow}^{\max} = 15$ kPa. The largest pore size occupied by oil before waterflooding is denoted R_1 . For clarity, waterfilled pores of configuration A are not shown. (a) Fluid distribution during waterfloods from different initial gas saturations for the cylindrical tubes. (b) Fluid distribution at different stages of the waterfloods for triangular tubes.

S_g , since water only invades oilfilled pores. These saturation dependencies does not occur in the corresponding simulations with cylindrical tubes as water invades both oil- and gasfilled pores initially, as demonstrated by Fig. 13(a) and Fig. 14(a). At larger water saturations, the scenario shown in Fig. 14(b) (bottom) occurs, and thus P_{cgo} depends strongly on two saturations. In this region, water invasion into the medium-sized pores contributes significantly to the increase of water saturation, implying that P_{cow} becomes strongly dependent on S_o in this region. A comparison with Fig. 14(a) shows that this relation is exact for cylindrical tubes since water invasion of the small oilfilled tubes does not occur in order of increasing pore size, as for the triangular geometry. The boundary between the large gas- and waterfilled tubes in Fig. 14(b) remains stationary, implying that P_{cgw} behaves as a function of only S_g . Furthermore, the calculated iso-caps show that the level of P_{cow} and P_{cgw} is higher in waterflooding of the triangular tubes, which is caused by the capillary behavior in Fig. 13(b).

Similar experiments are performed for the contact angles of case 3 with $P_{cow}^{\max} = 150$ kPa. In this case, the water content in the corners is very small, and thus we expect that the two models show better agreement. The same configuration changes occur in the triangular tubes as in the previous simulations with $P_{cow}^{\max} = 15$ kPa. However, the bulk pore occupancies in the bundle has become equal to the scenario for the cylindrical tubes shown in Fig. 12(a) and Fig. 14(a). Selected results are presented in Fig. 15. The gas-oil iso-caps calculated for gas injection reveal that P_{cgo} has become strongly dependent on S_o since bulk water is only present in the largest pores as in Fig. 12(a). The displacement paths and the gas-water iso-caps for the gas injections match correspondingly. The displacement paths for the waterfloods in Fig. 15(b) also show a better agreement. However, the triangular tubes yield a region at small S_w where P_{cgo} behaves as a function of only S_o . Thus, water invades some of the larger gasfilled pores before successively smaller oilfilled pores

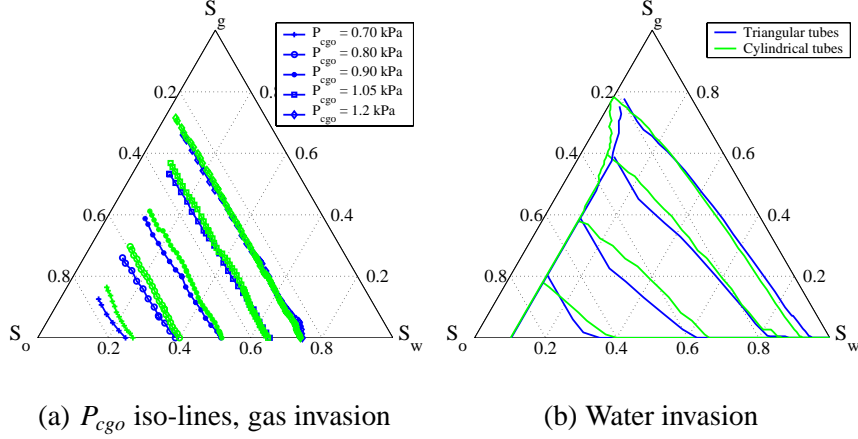
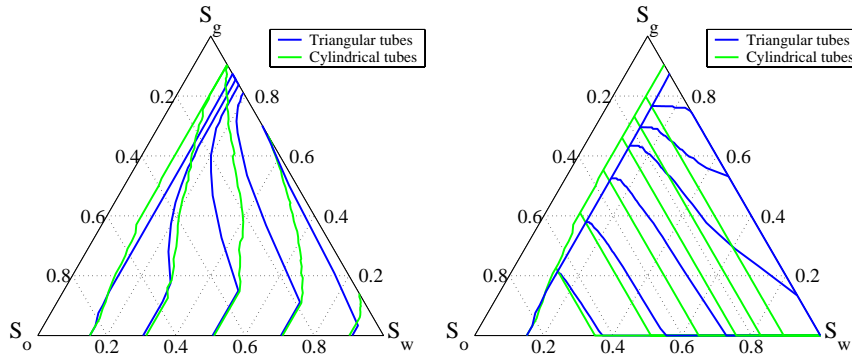


Figure 15. Results for triangular tubes (in blue) and cylindrical tubes (in green) with contact angles of case 3 and $P_{cow}^{\max} = 150$ kPa. (a) P_{cgo} iso-lines calculated from the gas injections. (b) Displacement paths for the waterfloods.

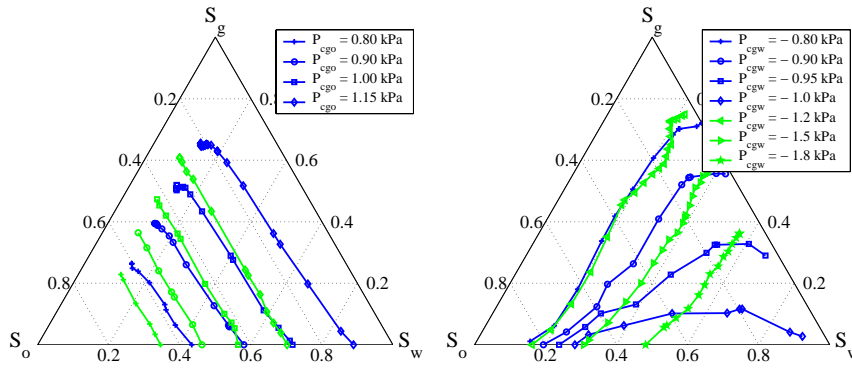
are invaded as well. This is caused by slightly higher entry pressures in the smaller gasfilled pores than in the larger oilfilled pores, as shown in Fig. 13(b). Notice also the large difference in capillary levels for the displacement from configuration C to D as compared to the case with $P_{cow}^{\max} = 15$ kPa in Fig. 13(a). The calculated iso-caps for the waterfloods are not shown here, but a good agreement between the two models is obtained, except for small S_w , where P_{cow} derived from the triangular tubes depends strongly on two saturations.

Results for the gas and water invasions with contact angles of case 2 and $P_{cow}^{\max} = 6.0$ kPa are shown in Fig. 16. Because of the small P_{cow}^{\max} value, configuration A remains present in a large amount of the smaller tubes in the invasion processes. At the different stages of imbibition where gas is injected, the configurations in the bundle of triangular tubes are arranged in order of increasing pore size as A–C–D for small S_w and as A–D–C–D for larger S_w . Gas invasion into configuration D is always a displacement to I, while water into configuration C is a displacement to I in the smaller tubes and to N in the larger tubes. Gas invades successively smaller oilfilled pores first, until invasion proceeds into successively larger waterfilled pores simultaneously, as demonstrated by the displacement paths in Fig. 16(a), and by the entry pressures in Fig. 17. The triangular tubes show a stronger decrease of S_w than the cylindrical tubes since the entry pressure for the displacement D to I does not decrease as much with decreasing pore size as the entry pressure for the equivalent displacements in the cylindrical tubes. Thus, a smaller range of capillary pressure is required for gas to invade large tubes of configuration D than for similar displacements in the bundle of cylindrical tubes. The displacement paths for the cylindrical tubes in Fig. 16(a) together with the calculated P_{cgo} and P_{cgw} iso-lines, presented in Fig. 16(c), (d), respectively, reveal the existence of region I for small S_g , where only P_{cgw} depends on two saturations, and region II for larger S_g , where only P_{cow} depends on two saturations. Thus, P_{cgo} is a function of only S_o in both regions.



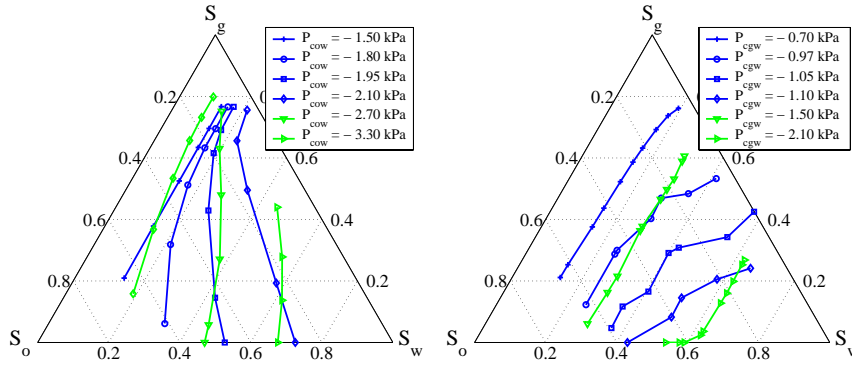
(a) Gas invasion

(b) Water invasion



(c) P_{cgo} iso-lines, gas invasion

(d) P_{cgw} iso-lines, gas invasion



(e) P_{cow} iso-lines, waterflooding

(f) P_{cgw} iso-lines, waterflooding

Figure 16. Results for triangular tubes (in blue) and cylindrical tubes (in green) with contact angles of case 2 and $P_{cow}^{\max} = 6.0$ kPa. (a), (b) Displacement paths for gas and water invasion. (c), (d) P_{cgo} and P_{cgw} iso-lines calculated for gas invasion. (e), (f) P_{cow} and P_{cgw} iso-lines calculated for water invasion.

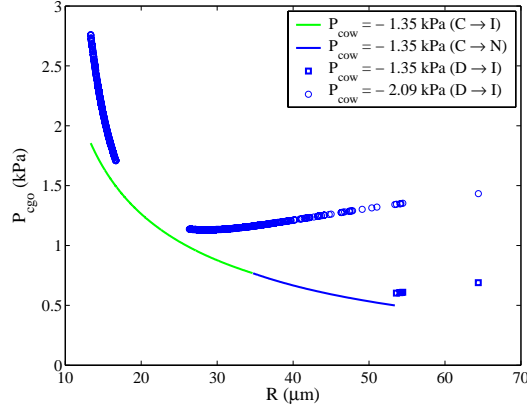


Figure 17. Gas-oil capillary pressure for the displacements in triangular tubes with contact angles of case 2 and $P_{cow}^{\max} = 6.0$ kPa. Gas is injected at $S_w = 0.1$ and $S_w = 0.7$.

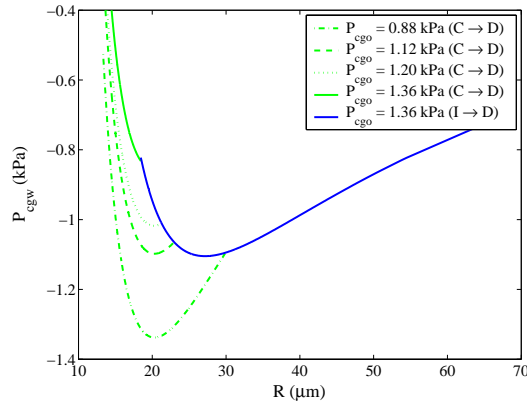


Figure 18. Gas-water capillary pressure as a function of pore size during waterflooding of the triangular tubes with contact angles of case 2 and $P_{cow}^{\max} = 6.0$ kPa.

As in previous simulations, the saturation dependency of P_{cgo} is violated for the triangular tubes since water also invades the smaller pore sizes in the preceding imbibition. This also causes P_{cgw} to become strongly dependent on two saturations in the entire saturation space. Furthermore, the level of P_{cgo} is slightly higher for the cylindrical tubes, while the level of P_{cgw} is higher for the triangular tubes, as in the previous simulations of gas injection.

Displacement paths for the waterfloods generated from different stages of the preceding gas injection are presented in Fig. 16(b). After the gas injections are terminated, the configurations are arranged in order of increasing pore size as A–C–N–I for small S_g . The displacements occurring are from configuration C to D, from I to D, and from N to I to D. The latter displacement represents collapse of the oil layers in configuration N before piston-like invasion, which is caused by increased water content in the corners during early stages of the waterfloods. The configurations are arranged as A–C–I–N–I when gas injection is terminated at large S_g , and the corresponding displacements are from C to D, from I to D, and from N to I to D. As shown in Fig. 16(b), the displacement paths from the bundle of triangular tubes can

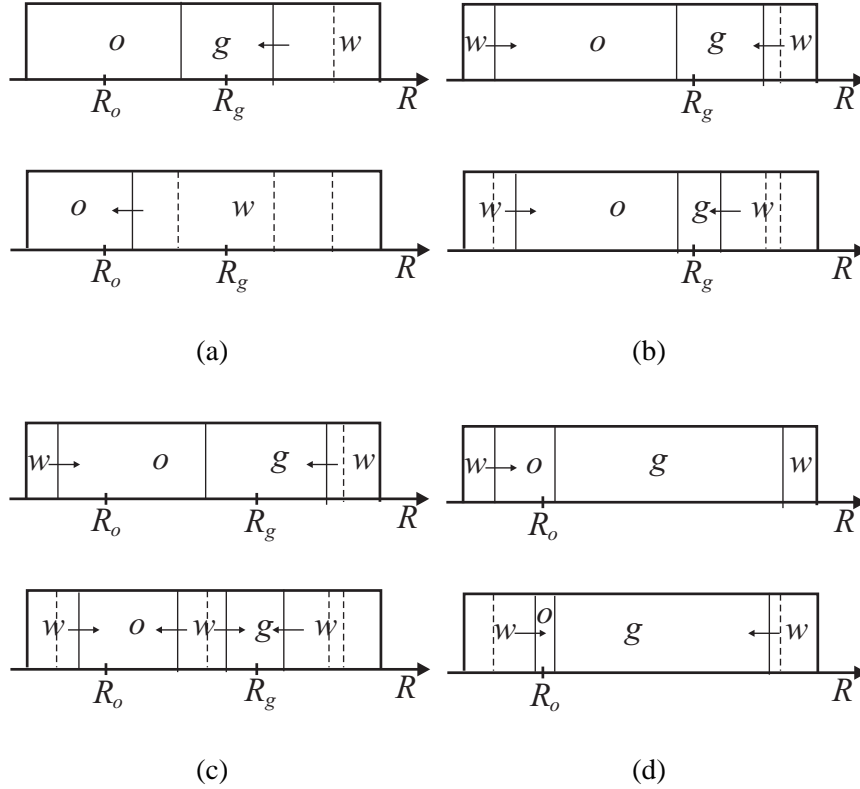


Figure 19. Bulk pore occupancies sketched at different stages of the waterfloods for contact angles of case 2 and $P_{cow}^{\max} = 6.0$ kPa. (a) Scenarios for cylindrical tubes. (b)–(d) Scenarios for triangular tubes when the initial gas saturation are (b) small, (c) medium, and (d) large. Waterfilled tubes of configuration A are not shown.

have a variety of shapes corresponding to different invasion orders. This is further manifested by Fig. 18 where the variations of P_{cgw} for the piston-like displacements occurring in the waterfloods are shown. In the bundle of cylindrical tubes, water first invades all the gasfilled pores in order of decreasing pore size, as illustrated by the pore occupancies in Fig. 19(a). Thus, P_{cgo} depends only on S_o , while P_{cgw} depends only on S_w in the cylindrical tubes. These dependencies agree approximately with the triangular tubes only for the waterfloods initiated from small gas saturations. This is because the change of water saturation by invasion into large gasfilled pores is more significant than the corresponding change by invasion into the smallest oil-filled pores, as illustrated in Fig. 19(b). The saturation dependencies derived from the triangular tubes change dramatically when waterflooding is initiated at intermediate and high gas saturations. Typical pore occupancies in these cases are shown in Fig. 19(c), (d). Since the positions of the gas-water and oil-water boundaries in Fig. 19(c) (bottom) may vary differently relative to each other for different initial gas saturations, the designated pore sizes R_o and R_g may be invaded by water at different saturation combinations, implying that all three capillary pressures are functions of two saturations. This is unlike the scenario depicted in Fig. 14(b), where the boundary between gasfilled and large waterfilled pores does not move,

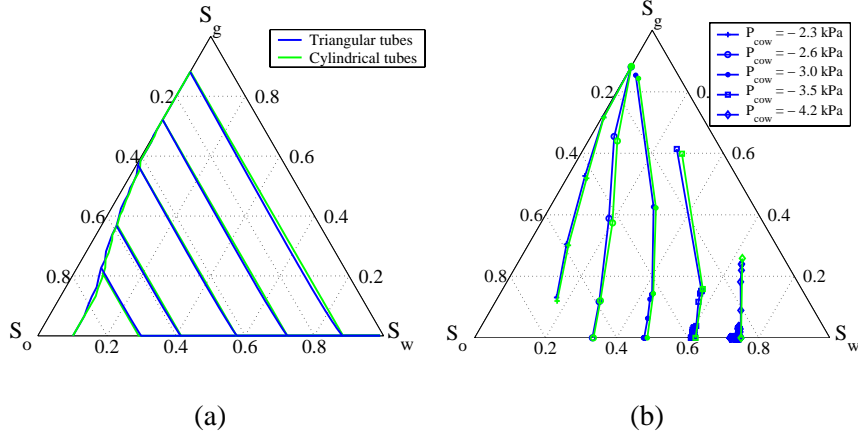


Figure 20. Results for waterflooding of triangular tubes (in blue) and cylindrical tubes (in green) with contact angles of case 2 and $P_{cow}^{\max} = 150$ kPa. (a) Displacement paths. (b) Calculated P_{cow} iso-lines.

and hence P_{cgw} behaves as a function of only S_g in that case. At high gas saturations, a larger amount of the small oilfilled pores are invaded first, as illustrated in Fig. 19(d) (top). This results in a small region where P_{cow} behaves as a function of only S_w , while P_{cgo} behaves as a function of only S_g . These significantly different behaviors of the two models during waterflooding are further elucidated by the calculated iso-caps presented in Fig. 16(e), (f). Differences are most noticeable in Fig. 16(f) where the P_{cgw} iso-lines for the cylindrical tubes track constant S_w , whereas the triangular tubes clearly deviate from this dependency at small oil saturations. As in the previous simulations, we find that the level of P_{cow} and P_{cgw} is significantly higher for the triangular tubes during waterflooding.

Corresponding experiments are simulated for case 2 when $P_{cow}^{\max} = 150$ kPa, and some selected results are shown in Fig. 20. After imbibition, configuration C has formed in the smaller tubes, while configuration E has formed in the larger tubes. Configuration A is absent since all tubes were invaded by oil in primary drainage. The displacements occurring in gas injection are from configuration C to I and N in the smaller tubes and from E to N in the larger tubes. In the subsequent water invasions the displacements C to D and E occur in the small tubes, while displacements N to E occur in the larger tubes. The pore occupancies at different stages of the waterfloods are compatible with the scenario shown in Fig. 19(a) for both models, resulting in an excellent agreement between the saturation dependencies and the level of capillary pressure during the sequence of invasion processes.

The results indicate that the presence of water in the corners of mixed-wet tubes may have a pronounced effect on the saturation dependencies of three-phase capillary pressures when contact angle hysteresis is assumed. The effect of hinging AMs in the corners during *two-phase* displacements is identified as the main reason why different saturation dependencies can occur in the triangular and cylindrical ge-

ometries. The fractions of water-wet and oil-wet area in a triangular tube vary with pore size. As a consequence, the saturation dependencies generated from the triangular tubes, with P_{cow}^{\max} fixed, may display trends similar to those derived from a bundle of cylindrical tubes with distributed contact angles (van Dijke and Sorbie, 2002a). Furthermore, the fraction of water-wet area in the triangular tubes, quantified in terms of b_{pd} , decreases as P_{cow}^{\max} is increased. Ma et al. (1996) derived the critical contact angle corresponding to zero entry pressure in the displacement from configuration C to D when $\theta_{owa} > \frac{\pi}{2}$:

$$\theta_{owa}^{\text{crit}} = \arccos \left[\frac{-b_{pd} \sin \alpha}{\frac{R}{\tan \alpha} - b_{pd}} \right]. \quad (70)$$

Thus, for small P_{cow}^{\max} , which corresponds to large $\theta_{owa}^{\text{crit}}$, we expect the saturation dependencies to agree more with water-wet conditions, e.g., with P_{cgo} as strongly dependent on S_g , see Fig. 10(b), (c). Similarly, for large P_{cow}^{\max} , which corresponds to smaller $\theta_{owa}^{\text{crit}}$, we expect the saturation dependencies to agree more with oil-wet conditions, e.g., with P_{cgo} as strongly dependent on S_o , see Fig. 15(a), (b). On the other hand, if $\theta_{owa} < \frac{\pi}{2}$, we do not expect the saturation dependencies to change according to P_{cow}^{\max} , since water always starts to invade the smallest pores. Thus, a good agreement between the saturation dependencies from cylindrical and triangular geometry is expected when contact angle hysteresis is absent, as in the work by van Dijke and Sorbie (2005).

7 Summary and conclusions

A bundle-of-triangular-tubes model has been developed for simulation of three-phase capillary pressure curves for mixed-wet conditions. Contact angle hysteresis leads to a diversity of different fluid configurations that can occur in the cross-sections during different sequences of the invasion processes. Algorithms are formulated to determine the actual displacements occurring for all combinations of receding and advancing contact angles, including the possibility of simultaneous displacement of the fluids present in the cross-section. Expressions for the corresponding capillary entry pressures are derived, accounting for hinging interfaces at fixed positions in the corners while the contact angle changes according to capillary pressure. This is an extension of the method proposed by van Dijke and Sorbie (2003) who considered three-phase entry pressure in angular tubes of uniform wettability.

The sequence of processes primary drainage, imbibition, gas injection and water-flooding are simulated for a specific set of interfacial tensions and three different combinations of contact angles representing oil-wet conditions with variable contact angle hysteresis. In these invasion processes, gas may invade configurations with oil layers bounded by bulk water and water in the corners (configuration E),

while water may invade configurations with oil layers bounded by bulk gas and water in the corners (configuration N). We have investigated if the three-phase entry pressures for such displacements are sensitive to the capillary pressures at the end of the preceding invasion process and to the capillary pressure at the end of primary drainage, P_{cow}^{\max} . The specific conclusions are as follows:

- (i) The gas-water capillary pressure, P_{cgw} , for gas invasion into configuration E, is more sensitive to variations of the oil-water capillary pressure, P_{cow} , than to variations of P_{cow}^{\max} . Furthermore, P_{cgw} increases with decreasing P_{cow} if $\theta_{gwr} < \frac{\pi}{2}$, while P_{cgw} decreases according to P_{cow} if $\theta_{gwr} > \frac{\pi}{2}$.
- (ii) The gas-water capillary pressure for water invasion into configuration N is less sensitive to variations of P_{cgo} than to variations of P_{cow}^{\max} for the range of capillary pressures where configuration N occurs.

The three-phase capillary pressure vs. saturation relationships calculated for the gas and water invasion processes are compared with corresponding results from a bundle-of-cylindrical-tubes model, using the constraint that the capillary pressures in primary drainage and the pore volumes are identical for both geometries. The specific conclusions are as follows:

- (i) For moderate levels of P_{cow}^{\max} , the two models may yield different saturation dependencies of three-phase capillary pressure. In the bundle of triangular tubes, *two* or even all *three* capillary pressures may depend strongly on two saturations in the same region of the saturation space, while the corresponding results from the bundle of cylindrical tubes often show that only one of the capillary pressures depend on more than one saturation in the same region.
- (ii) The different saturation dependencies derived from the bundle of triangular tubes result from capillary entry pressures that are affected by hinging interfaces in the corners when contact angle hysteresis is assumed. In general, these entry pressures predict different bulk pore occupancies than the simple Young-Laplace equation which is valid for the cylindrical geometry.
- (iii) The saturation dependencies derived from triangular tubes with P_{cow}^{\max} small, agree more with expected behavior for water-wet conditions, e.g., with P_{cgo} strongly dependent on S_g , while for high P_{cow}^{\max} , the results agree more with expected behavior for oil-wet conditions, e.g., with P_{cgo} strongly dependent on S_o . This is explained by a reduced area of water-wet surface when P_{cow}^{\max} is increased.
- (iv) The level of P_{cgw} and P_{cow} is generally higher for the triangular tubes than for the cylindrical tubes during the gas and water injections.
- (v) The saturation dependencies, capillary levels and bulk pore occupancies calculated from triangular tubes approach the corresponding results calculated from cylindrical tubes when the capillary level at the end of primary drainage is increased.

The results from this work indicate that three-phase capillary pressure correlations

for mixed-wet reservoirs should be formulated as functions of two saturations, as proposed by Helland and Skjæveland (2004b).

Nomenclature

A	Cross-sectional tube area
A_p	Total cross-sectional tube area in the bundle
b	Position of arc meniscus
C_s	Spreading coefficient
C_1, C_2, C_3	Coefficients in polynomial, see Eqs. (37)–(39) and Eqs. (61)–(63)
f	Pore-size frequency
I	Indicator notation, see Eq. (14)
L_s	Cross-sectional fluid-solid length
L_f	Cross-sectional fluid-fluid length
N	Total number of AMs present in a corner
P	Pressure
r	Radius of curvature
R	Radius of the inscribed circle
S	Saturation
W	Virtual work
x	Random number between 0 and 1
α	Corner half angle
β	Angle defined from geometry of the AMs in the corners
ΔF	Change of surface free energy
δx	Virtual displacement
η	Parameter in the Weibull distribution
θ	Contact angle
ξ	See Eq. (56)
σ	Interfacial tension

Subscripts

a	Advancing
c	Capillary
ch	Characteristic
g	Gas
h	Hinging
max	Maximum
min	Minimum
o	Oil
pd	Primary drainage
r	Receding

w Water

Superscripts

col	Collapse
crit	Critical
fin	Final
init	Initial
(<i>k</i>)	AM number counted in order from corner towards center
max	Maximum
X → Y	Displacement from configuration X to Y

Abbreviations

AM	Arc meniscus
MS–P	Mayer and Stowe – Princen
MTM	Main terminal meniscus
WAG	Water alternate gas

Acknowledgements

Support for Johan Olav Helland was provided by Statoil through the VISTA program.

References

- Bradford, S. A., Leij, F. J., 1995a. Fractional wettability effects on two- and three-fluid capillary pressure-saturation relations. *J. Cont. Hydr.* 20, 89–109.
- Bradford, S. A., Leij, F. J., 1995b. Wettability effects on scaling two- and three-fluid capillary pressure-saturation relations. *Env. Sci. Techn.* 29, 1446–1455.
- Bradford, S. A., Leij, F. J., 1996. Predicting two- and three-fluid capillary pressure-saturation relationships of porous media with fractional wettability. *Water Resources Research* 32 (2), 251–259.
- Diaz, C. E., Chatzis, I., Dullien, F. A. L., 1987. Simulation of capillary pressure curves using bond correlated site percolation on a simple cubic network. *Transport in Porous Media* 2, 215–240.
- Dong, M., Chatzis, I., 1995. The imbibition and flow of a wetting liquid along the corners of a square capillary tube. *J. Coll. Int. Sci.* 172, 278–288.

- Dong, M., Dullien, F. A. L., Chatzis, I., 1995. Imbibition of oil in film form over water present in edges of capillaries with an angular cross section. *J. Coll. Int. Sci.* 172, 21–36.
- Fenwick, D. H., Blunt, M. J., 1998. Three-dimensional modeling of three phase imbibition and drainage. *Adv. Water Resources* 25 (2), 121–143.
- Helland, J. O., Skjæveland, S. M., 2004a. Physically-based capillary pressure correlation for mixed-wet reservoirs from a bundle-of-tubes model. Paper SPE 89428 presented at the SPE/DOE Fourteenth Symposium on Improved Oil Recovery, Tulsa, OK, Apr. 17–21 .
- Helland, J. O., Skjæveland, S. M., 2004b. Three-phase capillary pressure correlation for mixed-wet reservoirs. Paper SPE 92057 presented at the SPE International Petroleum Conference in Mexico, Puebla, Mexico, Nov. 8–9 .
- Hui, M., Blunt, M. J., 2000. Effects of wettability on three-phase flow in porous media. *J. Phys. Chem. B* 104, 3833–3845.
- Kalaydjian, F. J.-M., 1992. Performance and analysis of three-phase capillary pressure curves for drainage and imbibition in porous media. Paper SPE 24878 presented at the SPE Annual Technical Conference and Exhibition, Washington, DC, Oct. 4–7 .
- Keller, A. A., Blunt, M. J., Roberts, P. V., 1997. Micromodel observation of the role of oil layers in three-phase flow. *Transport in Porous Media* 26, 277–297.
- Kovscek, A. R., Wong, H., Radke, C. J., 1993. A pore-level scenario for the development of mixed wettability in oil reservoirs. *Am. Inst. Chem. Eng. J.* 39 (6), 1072–1085.
- Ma, S., Mason, G., Morrow, N. R., 1996. Effect of contact angle on drainage and imbibition in regular polygonal tubes. *Coll. and Surf. A: Phys. and Eng. Asp.* 117, 273–291.
- Mayer, R. P., Stowe, R. A., 1965. Mercury porosimetry – breakthrough pressure for penetration between packed spheres. *J. Coll. Sci.* 20, 893–911.
- Morrow, N., 1975. The effects of surface roughness on contact angle with special reference to petroleum recovery. *J. Can. Pet. Tech.* 14 (4), 42–53.
- Piri, M., Blunt, M. J., 2002. Pore-scale modeling of three-phase flow in mixed-wet systems. Paper SPE 77726 presented at the SPE Annual Technical Conference and Exhibition, San Antonio, TX, Sept. 29–Oct. 2 .
- Piri, M., Blunt, M. J., 2004. Three-phase threshold capillary pressures in non-circular capillary tubes with different wettabilities including contact angle hysteresis. *Phys. Rev. E* 70 (061603).
- Piri, M., Blunt, M. J., 2005. Three-dimensional mixed-wet random pore-scale network modeling of two- and three-phase flow in porous media. I. model description. *Phys. Rev. E* 71 (026301).
- Princen, H. M., 1969a. Capillary phenomena in assemblies of parallel cylinders. i. capillary rise between two cylinders. *J. Coll. Int. Sci.* 30 (1), 69–75.
- Princen, H. M., 1969b. Capillary phenomena in assemblies of parallel cylinders. ii. capillary rise in systems with more than two cylinders. *J. Coll. Int. Sci.* 30 (3), 359–371.
- Princen, H. M., 1970. Capillary phenomena in assemblies of parallel cylinders. iii.

- liquid columns between horizontal parallel cylinders. *J. Coll. Int. Sci.* 34 (2), 171–184.
- Spildo, K., Buckley, J. S., 1999. Uniform and mixed wetting in square capillaries. *J. Pet. Sci. Eng.* 24, 145–154.
- van Dijke, M. I. J., Lago, M., Sorbie, K. S., Arujo, M., 2004. Free energy balance for three fluid phases in a capillary of arbitrarily shaped cross-section: capillary entry pressures and layers of the intermediate-wetting phase. *J. Coll. Int. Sci.* 277, 184–201.
- van Dijke, M. I. J., McDougall, S. R., Sorbie, K. S., 2001a. Three-phase capillary pressure and relative permeability relationships in mixed-wet systems. *Transport in Porous Media* 44 (1), 1–32.
- van Dijke, M. I. J., Sorbie, K. S., 2002a. An analysis of three-phase pore occupancies and relative permeabilities in porous media with variable wettability. *Transport in Porous Media* 48, 159–185.
- van Dijke, M. I. J., Sorbie, K. S., 2002b. The relation between interfacial tensions and wettability in three-phase systems: Consequences for pore occupancy and relative permeability. *J. Pet. Sci. Eng.* 33 (1–3), 39–48.
- van Dijke, M. I. J., Sorbie, K. S., 2003. Three-phase capillary entry conditions in pores of noncircular cross-section. *J. Coll. Int. Sci.* 260, 385–397.
- van Dijke, M. I. J., Sorbie, K. S., 2005. Consistency of three-phase capillary entry pressures and pore phase occupancies, paper submitted to *Adv. Wat. Res.*
- van Dijke, M. I. J., Sorbie, K. S., McDougall, S. R., 2001b. Saturation-dependencies of three-phase relative permeabilities in mixed-wet and fractionally wet systems. *Adv. Wat. Res.* 24, 365–384.
- Whitson, C. H., Brulè, M. R., 2000. *Phase Behavior*. Vol. 20 of Henry L. Doherty series Monograph / SPE. Society of Petroleum Engineers, Richardson, TX.
- Yang, S.-Y., Hirasaki, G., Basu, S., Vaidya, R., 1999. Mechanisms for contact angle hysteresis and advancing contact angles. *J. Pet. Sci. Eng.* 24, 63–73.
- Zhou, D., Blunt, M., 1998. Wettability effects in three-phase gravity drainage. *J. Pet. Sci. Eng.* 20, 203–211.
- Zhou, D., Blunt, M., Orr, Jr., F. M., 1997. Hydrocarbon drainage along corners of noncircular capillaries. *J. Coll. Int. Sci.* 187, 11–21.